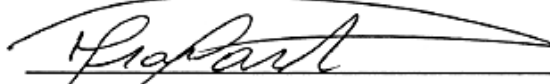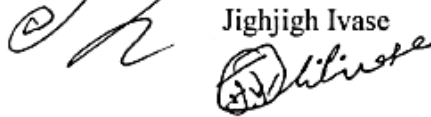# Attitude Determination and Control System for CubeSat

A Major Qualifying Project
Submitted to the Faculty of
WORCESTER POLYTECHNIC INSTITUTE
In Partial Fulfilment of the Requirements For The
Degree of Bachelor of Science
By

Assaad Farhat

Jighjigh Ivase

Ye Lu

Alan Snapp

Date: 1st March. 2013

Approved by:

Prof. Michael A. Demetriou, Major Advisor

Keywords:
1.) CubeSat
2.) ADCS

Abstract

This project continued the work on the development and testing of an Attitude Determination and Control Subsystem (ADCS) for a three-unit Cube Satellite mission led by WPI, the NASA Goddard Space Flight Center, and the Space Research Centre in Poland. This project focused on hardware selection in three areas: sensors, actuators, and processors. The attitude maintenance and control scheme was validated using numerical code written in MATLAB®. A secondary goal of the project was to outline a design for a test-bed where the control policies could be verified experimentally. This project developed a complete test-bed stand, leaving the construction portion for future ADCS teams, as well as recommendations for the parts to be used in the experimental section.

Acknowledgements

We would like to primarily thank our advisor:

Table of Contents

iii

Figures

Tables

Chapter 1   Introduction

For two years, WPI student project teams have been working on a design for a CubeSat system that will carry the payload of the SphinX-NG X-ray detector to monitor solar fluctuations. These teams have worked with the NASA Goddard Space Flight Center, the Space Research Center in Poland, and other polish universities to develop a mission plan and experiment parameters. The previous two years of projects outlined a simple structure sub-system with mechanical, thermal, and power considerations, as well as recommended many options for an attitude determination and control system. The focus of our project was selecting final components to be used in the CubeSat design, continuing to improve the control algorithms for the processor, and developing a plan to test the control algorithms in the lab.

1.1   Final Component Selection

A major portion of our project was dedicated to the research of satellite components, specifically components that could be used for the WPI CubeSat mission. This included both actuators, to maneuver the CubeSat, and sensors, to detect the orientation of the satellite relative to both the sun and the earth. The actuators were selected based on three key factors: mass, power required while operating, and their size, as the CubeSat has very specific sizing requirements. Sensors were chosen based upon their mass, size, and power as well, but more consideration was given to the accuracy of the component as the CubeSat mission outlined by previous work has stringent pointing requirements for science experiment.

1.2   Improving Control Algorithm

Another goal for this project was modifying the control code to both; accept the new sun sensor settings outlined by the Structural and Mission Analysis Subsystem team, as well as use the parameters for the new magnetorquer selected for actuation. Also, new methods of determining the gain values to be used during the different phases of the mission were researched so that the accuracy of the SphinX-NG could remain within two degrees of the sun vector for as long as possible.

1.3 Testing of Control Policies

The final portion of our project included research into work where a laboratory set-up on Earth used control algorithms for small satellites to control idealized versions of the control instruments that would be used in space. Using information from this research, another goal for this project was to develop a way that the control policies outlined by previous projects could be tested in the laboratory at WPI.

Chapter 2   Previous Work

Last year's CubeSat-ADCs team has already selected the control method and algorithm designs. For the control of the CubeSat, there are three phases after launch: de-tumbling, initial attitude determination and recursive attitude determination.

As the most prevalently used algorithms in satellite de-tumbling process, B-Dot controller controls the satellite by aligning it with the earth magnetic field vectors. Indeed, all small satellite used some variation of B-Dot as the controller for de-tumbling process [1] [2] [3].

As for initial attitude determination, TRIAD method is one of the earliest and simplest solutions to the spacecraft attitude determination problem. The method requires two sets of vectors: an observation vector from magnetometer and sun sensors, and a reference vector for each observation in terms of its inertial reference frame. Wahba's equation is also known as Error function. It is created to minimize errors when using TRIAD method. Different weights are applied to the each set of the sensors readings. The more accurate the sensor is, more weight is given. Immediately afterwards two solutions were offered to solve the problem: Davenport's q-Method and Quaternion Estimator Method (QUEST). Both of the methods use quaternion as an approach to optimize the result given by Wahba's equation [4].

As for recursive attitude determination, Extended Kalman Filter, [5] [6] [7]aka linear quadratic estimation, is a two-step process with a discrete time step. The sensors on satellite do not collect data continuously, so the Kalman filter is choose as it best incorporates the situation. Since most systems are nonlinear, the optimal estimate of Kalman Filter for linear system models is not the best solution. Extended Kalman filter (EKF) is used in satellites since it is the nonlinear version of the Kalman filter. EKF linearizes the system about an estimate of the current mean and covariance and produces an estimate of the future state.

In addition REQUEST method is a recursive version of Davenport's q-method that requires only one sensor reading. It is good for attitude maintenance during eclipse period since only the magnetic field measurements are available.

Chapter 3   Selecting Algorithm and Simulation Methods

3.1   Proposed Simulation Procedure for ADCS

The Attitude Determination and Control System (ADCS) comprise hardware such as sensors, actuators and the ADCS board which, in our case acts as the ADCS computer or processing unit. The ADCS also includes software that has been coded or programed into the ADCS computer. This software contains all the control schemes or algorithms of the ADC system. Therefore on a broad scale it can be observed that there are two major components that make up the ADCS – the hardware and software.

Due the unreliable nature of the inexpensive hardware and software that may be used in this project it is necessary to conduct simulations of hardware and software and indeed the entire ADCS in order to ensure that the system can cope with likely software and hardware failures. Therefore a possible software and hardware testing approach will be outlined here. Areas of testing that could be considered in these tests are situations of flawed sensor readings and actuator failures for instance. Also, the overall ADCS system operation should eventually be tested using air bearings and a test bed, such as the one being designed in this project, to better recreate conditions in the actual orbit or flight environment. A device, such as the Helmholtz coil, for producing uniform magnetic field should be considered to simulate the earth's magnetic field. An IEEE project that has attempted a similar approach shows an iterative procedure using Hardware-in-Loop and Software-in-Loop simulations where unsatisfactory results are re-run in the loop [8].
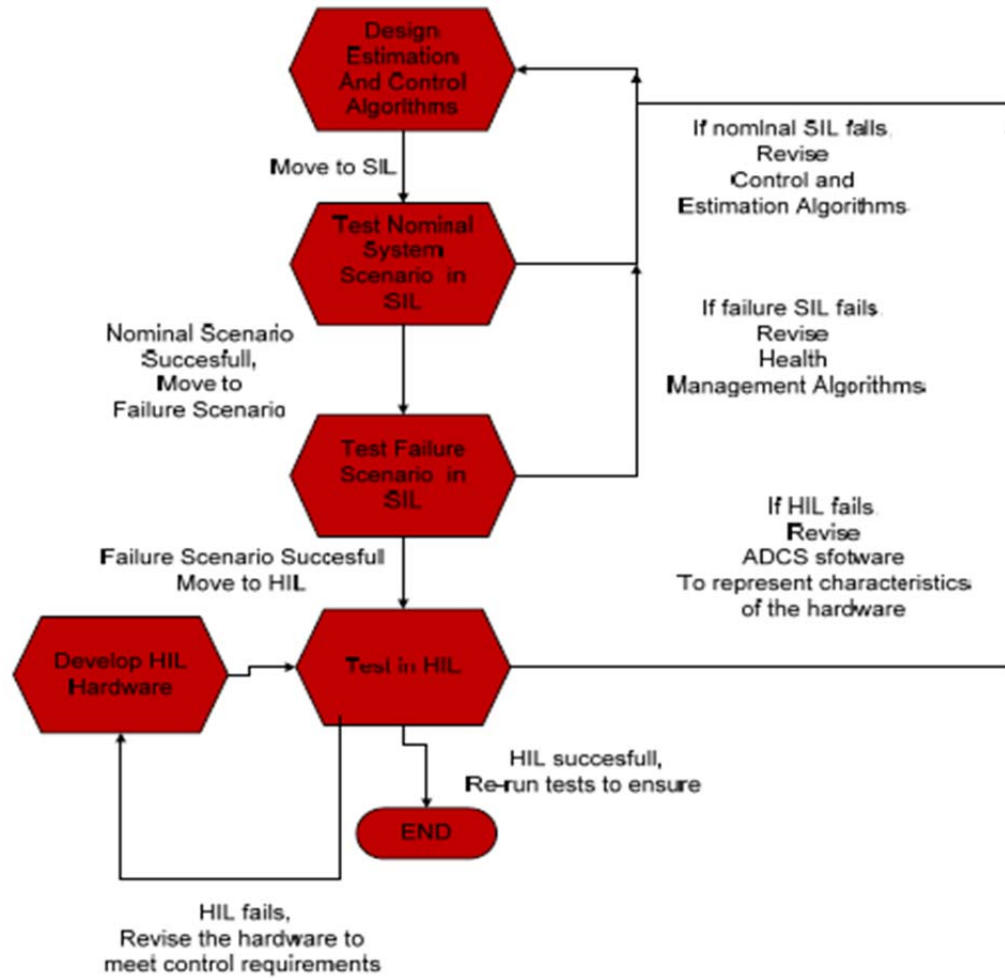
Figure 1: Iterative ADCS Design with SIL and HIL [8]

3.2 Explanation of Iterative Process Diagram

The ADCS design starts with the design of its control algorithms, for it is the control schemes that determine the type of software or hardware needed. These algorithms are then tested in an ideal setting with no induced error. Based on the results of our assessment or simulation, we can either return to the algorithm design phase to make necessary adjustments to our design or we can proceed. When we are satisfied with the results from our algorithms in the design phase and simulation, we can then go on to run the algorithms again, but this time, introducing errors to observe how the system will respond in a crisis situation [8].

After all software simulation is done, the appropriate hardware can be obtained and tested in simulation using the software.

3.3   Example: ADCS System Architecture Based on the ITU PSAT 2
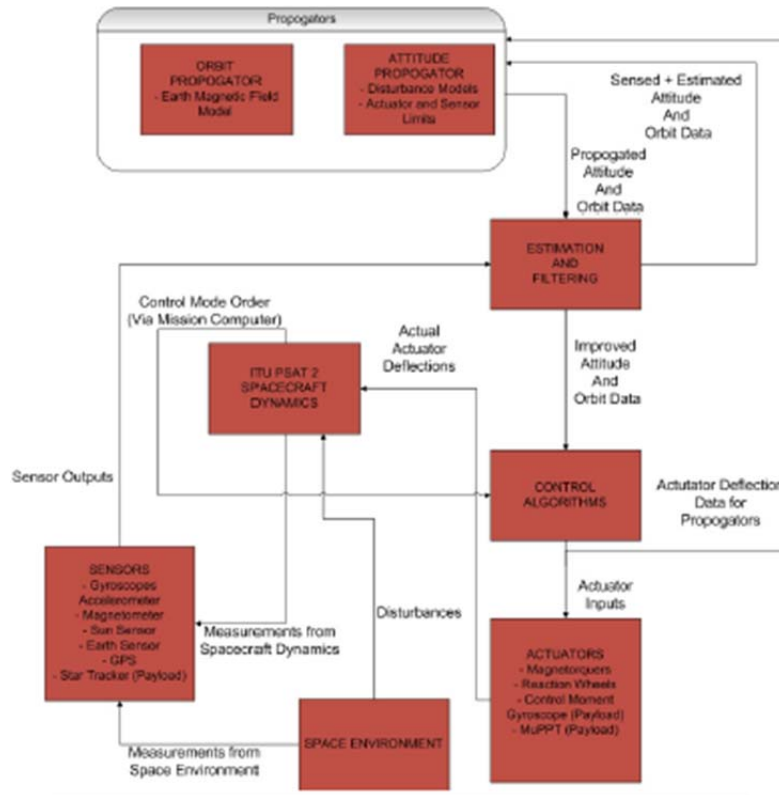
Figure 2: ADCS System Architecture [8]

Additional Components of ITU PSAT 2 System Architecture Include: Attitude Propagator, Orbit Propagator, Estimation and Filtering, Actuators [8].

3.4   Summary Procedure for Software Simulation

The ADCS algorithms should be tested on available software platform. Models for the attitude and orbit propagators can be generated from "Satellite Toolkit (STK)" since mathematical models generated by individuals for the both propagators may fail to emulate states or conditions of the mission actual mission. In addition since it is possible to extract the actual state data from STK we can see how well estimation layer works. ADCS software is provided either by an interface in STK or by some outside source, software receives state update from STK and noisy readings, magnetometer calibration errors, gyro biases, etc are applied to state vector to simulate actual sensor reading during mission [8].
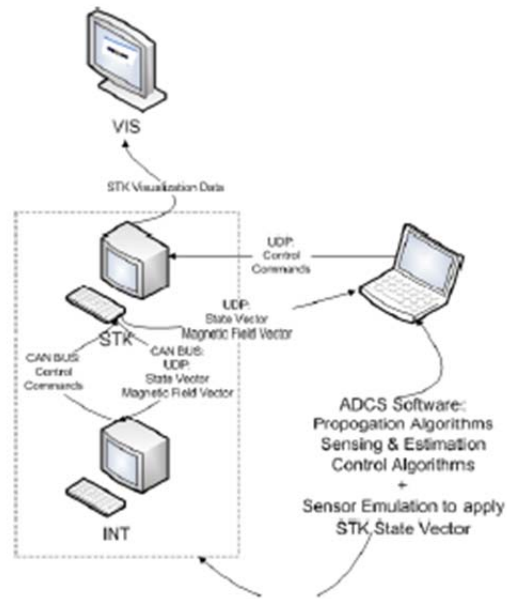
Figure 3: Example Software Simulation Setup [8]

3.5   Summary Procedure for Hardware Simulation

Hardware such as sensors, actuators and the on-board- computer also have to be tested in simulation with experimental platforms which will simulate the in-mission conditions of outer space. Such a setup is illustrated in the diagram below; where the rack system comprises two computers (PCs), a monitor to display simulation of satellite and a satellite hardware simulation system providing real responses to data.
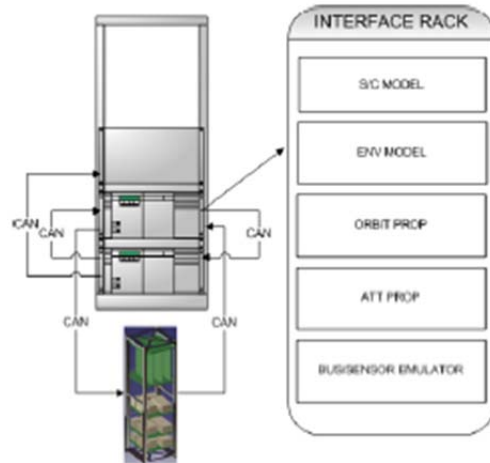
Figure 4: Hardware Simulation Setup [8]

3.6   B-Dot Stabilizing Controller

After ejection of the satellite in to orbit, it experiences varying angular velocities. For attitude determination to take place, the satellite has to be de-tumbled, in other words the angular velocities of the satellite must be made to approach zero.

The de-tumbling approach from last year was studied as well as the analysis of several types of de-tumbling algorithms and control policies. After identification of the de-tumbling methods, possible improvements to the current algorithms and methods were researched.

The stabilization phase is concerned with stopping random motion with no goal for a specific attitude orientation. A control policy called the B-Dot controller was the most prevalent method found in research on previous CubeSat missions. There are various policies that stabilize the spacecraft initially but most of these are variations of the B-dot control, based on Lyapunov functions.

3.7   Difference Quotient Method

The difference quotient method is the natural method to considering when dealing with differentiation of discrete signals. This method involves dividing the difference between measurements by the time interval between them. The value of the magnetic field at a point (k) could subtracted from the

value at a future point (k+1), in which case it is considered as the forward difference. In this case, the magnetic field value at (k) would have to be stored in order to be used in the differentiation. Alternatively, the magnetic field value at (k-1) could be subtracted from the value at (k). This is referred at to as the backward difference. In this method, the first two magnetometer outputs or discrete signals will have to be stored. Below are the expressions for the above mentioned methods:

Forward Difference:

$$\frac{B(k+1) - B(k)}{dt} \tag{1}$$

Backward Difference:

$$\frac{B(k) - B(k-1)}{dt} \tag{2}$$

Combining the two above approximations we get an improved one known as the central difference.

Central Difference:

$$\frac{B(k+1) - B(k-1)}{2(dt)} \tag{3}$$

where dt = time interval

For the case of the given magnetometer for this project, the difference quotient method found most appropriate to begin with is the backward difference which makes use of the present as well as the previous measurements to compute the derivative.

Magnetometer Characteristics
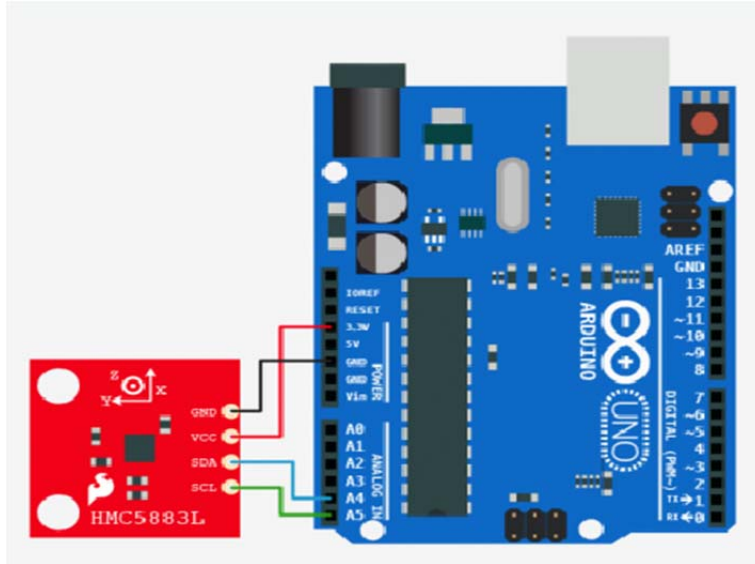
Figure 5: Honeywell's HM5883L:

The magnetometer chosen for the CubeSat is the Honeywell's HMC5883L Triple Axis Magnetometer with minimum and maximum sampling rates 0.75 Hz and 75 HZ respectively. It has a sampling interval of 0.006 seconds and a magnetic field output of ±1.16 gauss along the X and Y-axes, and ±1.08 gauss along the Z-axes.

Based on the minimum and maximum magnetometer output a cosine function was used to model magnetometer readings as $B(t) = 0.4 \cos(t) + 1.12$. The derivative was then computed analytically and by using the difference quotient method and both results were compared.

Comparing both derivatives at a high sampling interval to show differences
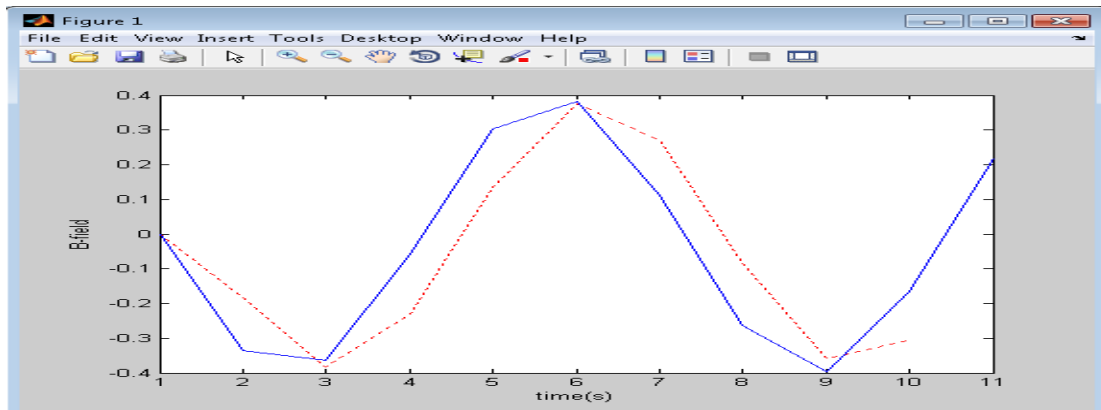
Figure 6: Matlab plot of derivatives by both methods.

In red = dB/dt: using difference quotient method: $\frac{d(B)}{dt}$ = -0.4sin(t)

In blue = dB/dt: found by solving analytically: dB/dt = -0.4sin(t)

The difference quotient method is developed from the Taylor series approximation therefore the errors that arise due to their use are also based on the same Taylor series approximation and also depend on the time interval (dt). The errors are as follows:

For the forward difference: $e_f = -\frac{dt}{2!}B''$

Where B'' = the 2nd derivative

For the backward difference: $e_b = \frac{dt}{2}B'' + \frac{(dt)^2}{3!}B'''$

Where B''' = the 3rd derivative

For the central difference: $e_c = -\frac{dt^2}{3!}B'''$ [9]

3.8   Nyquist Sampling Theorem

Another method that was considered was differentiation using the Nyquist sampling criterion. This method is described in the article for differentiation of Multi-dimensional signals by Farid and Simonelli [10]. The theorem states that a function with a limited upper frequency can be reconstructed from an infinite sequence of samples spaced at half the sampling rate or with a bandwidth no greater than the sampling rate. This method is used to differentiate a continuous signal that is interpolated from the initial discrete signal. This interpolation is done by using the ideal interpolator function s_T (also called the sic function). This is based on the assumption that the discrete signal was obtained by sampling an original continuous function containing frequencies no higher than $\frac{2\pi}{U}cycles/length$ at a sampling rate of $\frac{U\,samples}{length}$ [10].

Using the above assumption the Nyquist sampling theorem implies that the continuous signal may be reconstructed from the discrete signal as the following samples:

$$f(x) = \sum_k f[k] \cdot s_T(x - kU)$$

<div align="right">(4)</div>

Continuous signal derived from the given discrete signal [10].

Where: $s_T(x) = \dfrac{\sin(\pi x/U)}{\pi x/U}$ this is the continuous ideal interpolator of "sinc" function

        f(x) : the continuous time signal

        f[k] : the discretely sampled counterpart

Assuming that the continuous signal equation above converges, we can then go ahead and differentiate the continuous function on both sides of the equation.

The derivative operator will only be applied to continuous functions, $f(x)$ and $s_T(x)$

Let "D" be the derivative operator [10]

$$D\{f\}(x) = \sum_k f[k] \cdot D\{s_T\}(x - kU)$$

$$= \sum_k f[k] \cdot d(x - kU)$$

<div align="right">(5)</div>

Where: $d(x)$ the derivative of the sine function

$$d(x) = \frac{\pi^2 x/U\cos(\frac{\pi x}{U}) - \pi/T\sin(\frac{\pi x}{U})}{(\pi x/U)^2}$$

Arrive at a definition of discrete differentiation by sampling both sides of the above equation on the original Sampling interval. If the original sampling interval is "n" and the sampling rate is "T" we have:

$$
\begin{aligned}
\mathcal{D}\{f\}[n] &\equiv \mathcal{D}\{f\}(x)|_{x=nT} \\
&= \sum_k f[k] \cdot d((n-k)T) \\
&= \sum_k f[k] \cdot d_T[n-k],
\end{aligned}
\tag{6}
$$

Where dT is the T-sampled sinc derivative.

Accurate Implementation of this method requires very large filters.

After considering and exploring the appropriate options for differentiation of discrete signals, the next task is to design appropriate filters for these for the chosen method of differentiation. Kalman filters can be used to estimate the discrete time sequence governed by the difference equation of the system we are considering. After desired constraints have been set, derivative filters can then be designed for a given order and length.

Chapter 4   Sensors and Actuators Selections

4.1   Comtech AA Coarse Sun Sensor
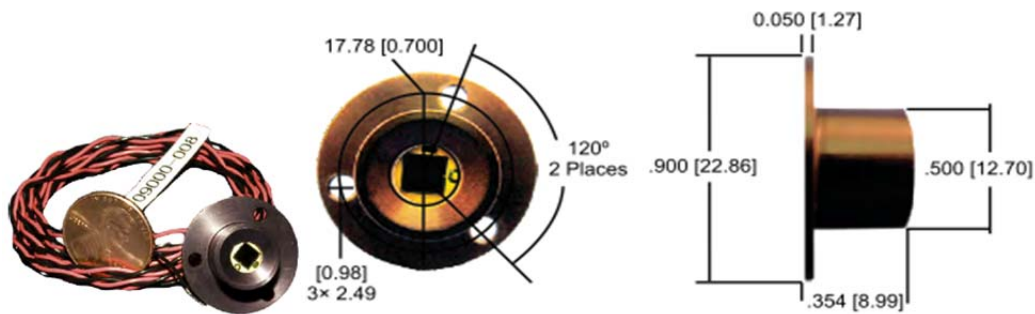
Figure 7: Dimension of Coarse Sun Sensor

Sun sensors, although mass-produced according to listed specifications, contain minute differences in photodiode angles and sensitivities that necessitate calibration for use in space. The goal of the data from the Coarse Sun Sensor (CSS) which are located along the sides of the satellite is to allow Attitude Determination & Control (ADC) to determine the Angle of Incidence (AOI) and make attitude adjustments to bring the view of the Sun. The AOI varies at 15° increments because the CSS requires only a coarse view of which direction to turn and then the Fine Sun Sensor (FSS) data will allow for finer adjustments. The CSS data are symmetrical and include voltage outputs that could correspond to either a positive or negative AOI. The Field of View (FOV) of the CSS at the bottom of the satellite overlaps with the FOV of those mounted on opposing sides, telling the ADC which AOI the voltage corresponds to base on whether or not the CSS at the base shows a voltage output.

The following table provides the CSS data and specification [11].

Table 1: Data and Specifications of Coarse Sun Sensor

Flight Heritage	ALEXIS, HETE, MOST, ChipSAT and STPSat-1
Field of View (FoV)	120° full-angle circular field of view
Accuracy	3sigma $\pm$5° of 1-axis knowledge
Power	None required
Volume	1.27 cm diameter x 0.90 cm height
Mass	10 g w/ 1.27m flying leads
Size	Housing diameter: 1.27 cm Flange diameter: 2.286 cm Sensor height: 0.899 cm
Bandwidth	100KHz
Operating Temperature	-40°C to 100°C
Vibration Test Levels	14.1g rms protoqual (testing procedure)
Shock Test Levels	60g protoqual
Radiation (TID)	>1 Mrads
Materials	Epitaxial Silicon (help makes the sensor radiation hardened)
Price	$2,641.4 US per 1 $13,207 US per 5

4.2   SSBV CubeSat Sun Sensor

Figure 8: Fine Sun Sensor

The Fine Sun Sensor (FSS) data allows ADC to make minute attitude adjustments, allowing the adjacent solar array to maximize solar power generation. The threshold orientation accuracy for the satellite is 5°. ADC required calibration data that would allow for fine adjustment: the data set included 10° increments along the entire FOV and 2° increments surrounding the region normal to the sensor mounting surface [12].

The FSS has four individual diodes canted towards the sensor's quadrants, each receiving voltage outputs. A potential application of the data is to relate x angle, y angle and voltage by processing calibration data into a 3D surface. By orienting these surfaces to correspond to sensor setup, ADC could generate contour projections of AOI based on on-orbit voltages. The intersection of these projections would be the satellite's attitude relative to the Sun.

The following table provides the FSS data and specifications:

Table 2: Data and Specifications of Fine Sun Sensor

Flight Heritage	UKube-1 and TDS-1 satellites in 2012
Mass	$< 5 \, g$
Power	$< 5 \, mA$
Size	33mm x 11mm x 6mm
Operating temperature	-25°C to +150°C
Field of view	120°
Update Rate (Bandwidth)	$> 10Hz$
Accuracy	$< 0.5°$
Power Supply	3.3 or 5 V
Interface	I/F: 4 analogue channels, 9-way Nano-D Connector
Material	Aluminum & Titanium
Price	$5,000 US

To capture the necessary calibration data, the sensors were tested using a Calibrated AM0 Sun Simulator light source at varying angles of incidence, recording voltage output from the photodiodes at each position. The sensors were also tested across a range of temperatures to see if there is performance variation within the company's listed temperature range.

4.3   EVAL-ADXRS450Z-M Gyroscope
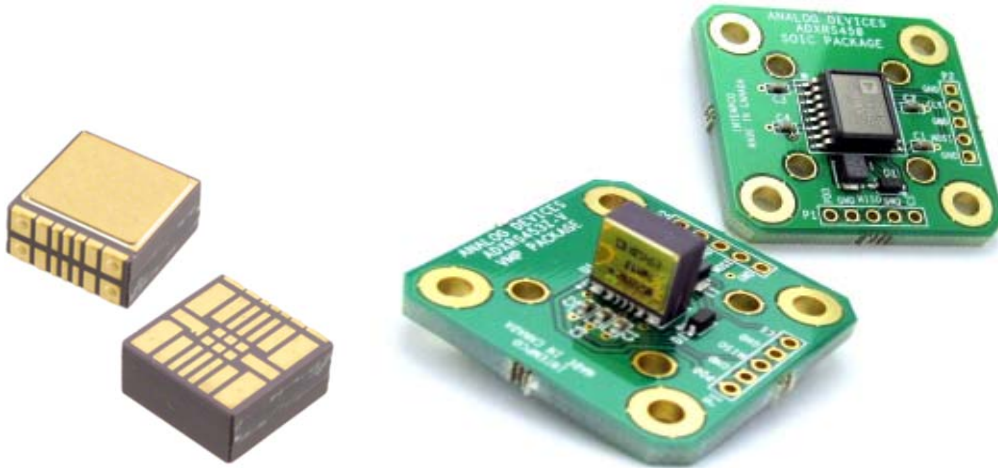
Figure 9: Gyroscope

The EVAL-ADXRS450Z-M is a simple breakout board that enables easy connection of an ADXRS450 into an existing system. The EVAL-ADXRS450Z-M is a digital-output, single-axis gyroscope with built-in temperature calibration [13].

The ADXRS450 is available in two packages: an SOIC package for yaw-axis rate sensing, and a vertical-mount package (VMP) for pitch- or roll-axis sensing. In applications requiring multi-axis sensing, the innovative VMP greatly simplifies assembly by eliminating the need for additional boards mounted at 90°. An advanced, differential, quad sensor design rejects the influence of linear acceleration, enabling the ADXRS450 to operate in exceedingly harsh environments where shock and vibration are present [14].

The ADXRS450 uses an internal, continuous self-test architecture. The integrity of the electromechanical system is checked by applying a high frequency electrostatic force to the sense structure to generate a rate signal that can be differentiated from the baseband rate data and internally analyzed.

The ADXRS450 is capable of sensing angular rate of up to ±300°/sec. Angular rate data is presented as a 16-bit word, as part of a 32-bit SPI message. The ADXRS450 is available in a cavity plastic 16-lead SOIC (SOIC_CAV) and an SMT-compatible vertical mount package (LCC_V), and is

capable of operating across both a wide voltage range (3.3 V to 5 V) and temperature range (−40°C to +105°C).

The following table presents all the ADXRS450 specifications and pin connections:

Table 3: Specifications of Gyroscope

Operating Temperature	-40°C to 105°C
Sensitivity	80 LSB
Typical Bandwidth	80 Hz
Voltage Supply	3.15V to 5.25V
Board Size	33mm x 33mm x 1.2mm
Price	$59.54 US
Material	Aluminum & Titanium
Connect	Main Computer
SPI digital output with 16-bit data-word	
Internally temperature compensated	
Complete rate gyroscope on a single chip	
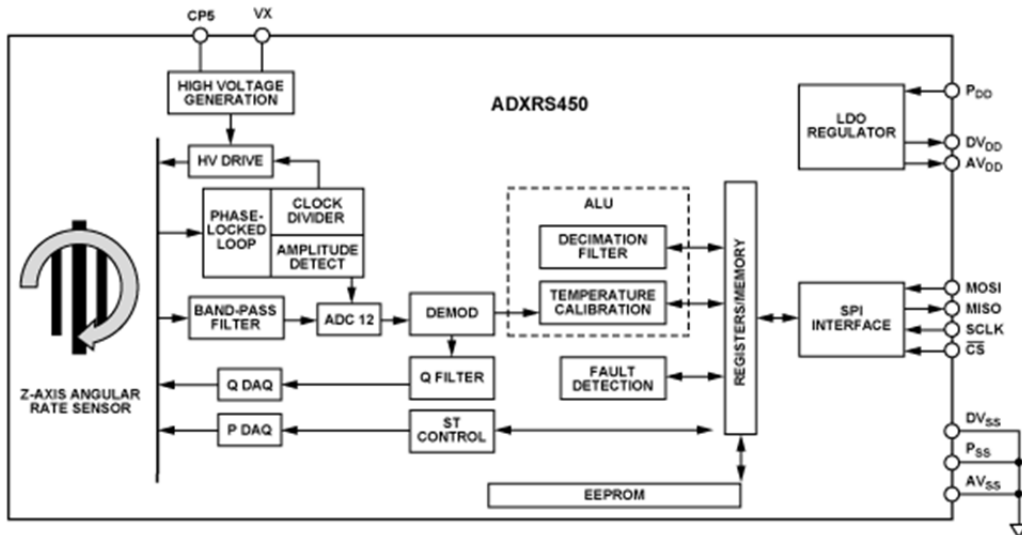
Figure 10: Gyroscope Pin Connection

4.4 Magnetometer

Figure 11: Magnetometer

Table 4: Data and Specifications of Magnetometer

Size	17.78X17.78X0.9mm
Mass	18 mg
Operating Temperature	-30-85 C
Heading Accuracy	1-2 Degree
Linearity	$\pm 0.1\%$
Measurement Period	6ms
Supply Voltage	2.16-3.6V
Max Current Draw	6 µA
Rate	100 KHz or 400 KHz
Price	14.95$
Materials	Nickel-Iron Permalloy

Last year's Design and Analysis project outlined a Magnetometer created by Honeywell, a leader in the sensor/detector industry. This component satisfied three of the four design guidelines set forth by

20

the first Design and Analysis team from 2011 [1]. The Magnetometer selected is the HMC5883L 3-axis sensor, with a suggested breakout board built by SparkFun. This magnetic sensor had excellent flight heritage, measured all 3 axis, and operates in the 3.3V range. Also, the component has a very low cost.

Taking the HMC5883L as a baseline, initial research was done to see if there were any new components made by the same company, or similar parts made by a different company. The Honeywell Company touted the HMC line as the 'premiere sensors' in the field. The Freescale FXOS8700CQ: 6-Axis Xtrinsic Sensor, a component combining an accelerometer and magnetometer, was looked at, but determined to be much too heavy, with a lesser accuracy for the magnetic measurements. Also, the power requirements were much greater to power both types of sensors [15]. The HMC5883L was again selected as the most viable option because of its accuracy, weight, and flight heritage.

Two mounting options were presented by last year's Design and Analysis team for the magnetometer. The first was a static option, where the sensor was on the top +Z face of the design, with its axis aligned with the body axis of the CubeSat. This option is mechanically simple, cheap, and does not create any torques or disturbances during normal use. The second option was to use a boom-style solar panel deployment to get the sensor as far away from the rest of the electric components as possible. This approach is mechanically complex, and required additional analysis done to acquire inertial measurements. However, after restrictions from the P-POD document were discussed, it was realized that a deployable sensor would not be practical for our design as the sensor would have to remain un-deployed for thirty minutes after the ejection of the CubeSat from the launch vehicle. The magnetometer is necessary for initial de-tumbling functions, and thus waiting thirty minutes to begin to de-tumble would vastly increase de-tumbling time. Thus, the top surface mounting option was selected because of the ease of integration and the simplicity of the design.

The Magnetometer would need to have its data output conditioned by its own breakout board, and then sent, under last year's specifications, to the main computer [16]. From last year's design, the Clyde-Space Mission Interface Computer was suggested as the main computer for the WPI mission. This motherboard is integrated with pluggable processor modules (PPMs), which allow direct connection from

the sensor output to the computer. The Clyde-Space component was selected because of its two types of

PPMs, one for high performance data handling (the ARM922T), and one for low power requirements and

redundancies (the MSP430). The HMC5883L would be connected to ARM922T module, as the

magnetometer can output data up to 400 Hz.

4.5   Magnetorquer Selection
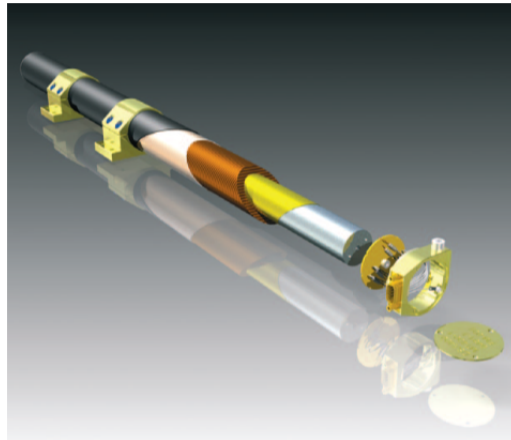
Figure 12: Magnetorquer

After testing three types of magnetorquers last year, the ADC team determined that the best possible component for the WPI mission would be the ZARM MTO.2-1 Magnetorquer [1]. This component had the lowest mass, size, and power requirements of all the types tested, and reached the magnetic moments required with a low power requirement and much less weight. The Zarm Technik Corporation was contacted for more information about their MTO.2-1; however they had discontinued the MTO.2-1 product line. Zarm suggested the possibility of using a MTO.5-1, which was one of the other products tested by last year's team. This piece reaches the same magnetic moments as the MTO.2-1, but at a much lower power cost. However, the MTO.5-1 is longer, heavier, and more expensive than the MTO.2-1, but given that there are no other viable options, the MTO.5-1 has been selected as the magnetorquer of choice for the WPI mission.
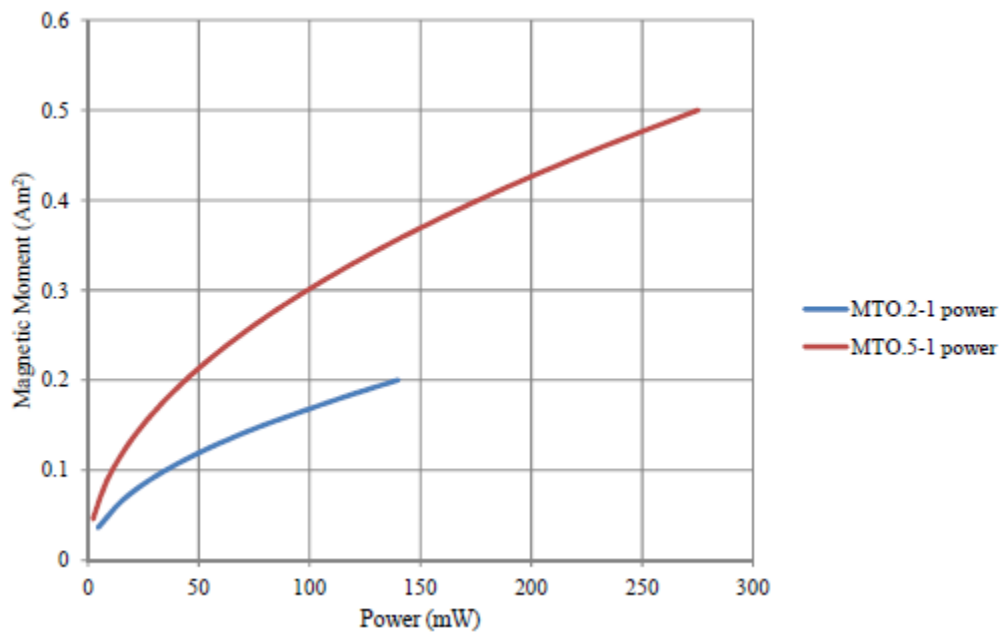
Figure 13: Magnetorquer Power and Moment Output Comparison

4.6   Clyde-Space ADCS Command Board

Figure 14: Clyde-Space ADCS Board

In researching new magnetometers and magnetorquers, the Clyde-Space ADCS board was

discovered. This is a new product made by Clyde-Space, a trusted and prominent company in the CubeSat

industry. This component would serve as a command hub for the systems involved with de-tumbling and

attitude determination/control. With PPM interfaces for multiple sensors, including but not limited to;

coarse and fine sun sensors, GPS systems (an included GPS daughter board is optional), and gyroscopes.

The advanced version of the board comes with it's own included magnetometer, but the company has

stated that it is a modular component and could be removed depended on the design constraints specific to

each user. This board could be connected to a PPM on the main computer, and would control the sensors

and actuators connected to it, while sending the necessary information to the main computer. Clyde-Space

has embedded programs in the board, such as de-tumbling and sun tracking, but also states that the board

has the ability to accept custom MatLab coding [17]. All 5 of the CubeSat sun sensors, as well as the

GPS, gyroscope, and magnetometer, will be connected and feeding information to the ADCS board,

which will be directly controlling the actuators using the information being fed to it by the sensors.

4.7 Summary of Final Hardware Selection

Table 5: Final selections of Hardware

Sensor/ Actuator	Model	Manufacture	Number Needed	Total Price	Power Requirement
Sun Sensor	Coarse	Comtech AA	4	$10,566	None
Sun Sensor	Fine	SSBV Space and Ground Systems	1	$5,000	< 140 mW
Magneto-meter	HMC5883L	Honeywell	1	$14.95	0.25 mW
Gyroscope	ADXRS450	Analog Devices	1	$59.54	30 mW
Magnetic Torquer	5-1 PO	Zarm Technik	3	Unknown	275 mW

Materials employed included dissipative paints, indium-tin-oxide films, carbon loaded polymers, thin SiOx coatings on metallic substrates, Nickel-Iron Permalloys, and conductive tapes.

Chapter 5   Model and Sensors Readings

The goal of the attitude determination and control system is to develop comprehensive system and algorithms that the CubeSat can use for its state control, stabilizing and mission required maneuvers. In order to achieve this goal, acquiring accurate information from geomagnetic model, sun sensor, magnetometer, and gyroscopes readings is significant for the CubeSat to perform control algorithms.

5.1   Geomagnetic Model

Geomagnetic model is an important piece of information for the CubeSat because it is one of the reference fields which will be used in the control algorithm. The values from geomagnetic model will be compared with magnetometer readings in order to determine the CubeSat's state which will then be used to control he magnetorquer output. Three geomagnetic field models are available for use.

5.1.1   High Definition Geomagnetic Model (HDGM)

It is provided by US National Geophysical Data Center for high accuracy geomagnetic referencing. This model includes the main geomagnetic field, crustal field to degree 720 and also secular variation. This model significantly reduces geomagnetic referencing errors. It is updated each year. But the model is priced at $19,997 per year [18].

5.1.2   International Geomagnetic Reference Field 11th generation (IGRF)

As selected by last year's ADC team, this model holds adequate accuracy as indicated by the mission requirements. This model is also used by Satellite Tool Kit (STK) for geomagnetic field reference [19]. It is updated every five years. The detailed descriptions and calculations of magnetic field vector can be found in CUBESA-ADC12.

5.1.3   World Magnetic Model (WMM)

This is an alternative geomagnetic model. It is not as accurate as IGRF. As our mission does not require high accuracy of the attitude, WMM is optional as the computational time is less than that of the

IGRF. The strength of the magnetic field changes over time. According to the data from WMM 2010-2015, the greatest change in magnetic field strength is about 90 nT/yr [20]. Compare the error produce by the models with the magnetic strength shift, it is well within the tolerance. WMM models the geomagnetic field in the following way:

$$B(r,t) = B_{core}(r,t) + B_{crust}(r) + B_{disturbance}(r,t)$$

The geomagnetic field varies in space and time. B_{core} is the dominating part of the field. It accounts for 95% of the total field strength. B_{crust} is much smaller when compared with B_{core}. This field cannot be modeled with low degree spherical harmonic models therefore is excluded in WMM. B_{crust} models the field from magnetized crustal rocks, so it's not useful in determining the magnetic field in the space. $B_{disturbance}$ arises from varies resources such as ionosphere and magnetosphere. It varies with time and space [20].

The advantage of WMM is that it is implemented in the latest version of MATLAB (MATLAB 2012b). If we have the processor that can run MATLAB script, it's very convenient to use WMM instead of IGRF.

5.2   Sun Sensor Reading

The selections of both fine and coarse sun sensors were finalized. The top unit in the 3U-CubeSat is occupied by the mission payload and it is not accessible for any purposes, therefore, the original design of 5 plus 1 sun sensor setting came down to only 4 plus 1, which means only 4 coarse sun sensors will be used in addition to one fine sun sensor. The selected coarse sun sensors provide only one-axis information about the Sun's position; in other words, the Sun's position cannot be determined accurately with the one-axis sun sensors. As a result, a rough estimation of the Sun's position is required to effectively control the CubeSat. The following table indicates the detailed methods of estimating the Sun's position.

Table 6: Method of Sun Sensor Reading

Available face(s) of sun sensor reading	Phase angle [degrees]		Sun Position vector in Body frame
	θ	ψ	
+X	0	90	$(1, 0, 0)$
-X	180	90	$(-1, 0, 0)$
+Y	90	90	$(0, 1, 0)$
No sensor reading	270	90	$(0, -1, 0)$
-Z	0	180	$(0, 0, -1)$
+X,+Y	45	90	$(\sqrt{2}/2, \sqrt{2}/2, 0)$
+X,-Z	0	135	$(\sqrt{2}/2, 0, -\sqrt{2}/2)$
-X,+Y	135	90	$(-\sqrt{2}/2, -\sqrt{2}/2, 0)$
-X,-Z	180	135	$(-\sqrt{2}/2, 0, -\sqrt{2}/2)$
+Y,-Z	90	135	$(0, \sqrt{2}/2, -\sqrt{2}/2)$
+X,+Y,-Z	45	135	$(0.5, 0.5, -\sqrt{2}/2)$
-X,+Y,-Z	135	135	$(-0.5, 0.5, -\sqrt{2}/2)$

The +Z face is pointing to the sun. Whenever the reading from +Z face is available, which is the reading from the fine sun sensor, it will be taken as a prior value and any readings from other coarse sensors will be ignored. The method of estimation primarily assumes that if the sun sensor on only +X face has readings, the Sun's position is considered to be aligned with the +X axis and if sun sensors on both +X and +Y faces have readings, then the Sun's position is considered to be aligned with 45 degrees from both +X and +Y direction and so the same for all others. Notice that there is no –Y face because only 4 coarse sun sensors are used. "No sensor reading" indicates that none of the 5 sun sensors on board has sight of the Sun, so the Sun is assumed to be at the –Y phase. Since the mission design group will be providing detailed orbital information, then the information on whether or not the CubeSat is during eclipse is known. As a result, it's adequate to assume if the CubeSat is known to be in lighting period,

then the "no sensor reading" indicates the Sun is in the –Y face. With the list of all possible phase angles

the Sun's position vector in the body frame then can be calculated and thus be used in the control

algorithms.

5.3 Alternative Determination Methods

Provided by the Hubble Space telescope, four of its six world class gyros failed. And there are

several known cases where the gyro failed during mission. In order to secure our mission, back up

determination algorithms should be kept on board in case of parts' failure.

5.3.1 Magnetometer-Only Deterministic Attitude/Rate Determination

This method was previously used on Solar, Anomalous, and Magnetospheric Particles Explorer

(SAMPEX) which is a small explorer spacecraft. It has been found that the algorithm is effective of

yielding accuracy of 1.5 degree in attitude and 0.01 degree/second in rates. This Method can be used as a

back-up algorithm in case the gyroscope failed during the mission [21]. This algorithm allows us to

determine the angular rate of the CubeSat.

The deterministic scheme constructs second vector measurement from the 1st derivative of B

resolved in the reference and body frames. The transformation equations are given below:

$$A\vec{B}^R = \vec{B}^A$$

$$A\dot{\vec{B}}^R = \dot{\vec{B}}^A + \vec{\omega}^A \times \vec{B}^A \tag{7}$$

Where A is the attitude matrix, $\vec{\omega}$ is the angular velocity vector, and R and A represents reference

and body frame respectively [21].

Along with the deterministic attitude determination from magnetometer-only data, Real-Time Sequential Filter (RTSF) is used for accurate determination and faster convergence.

5.3.2   State Determination with Failed Gyroscope

The Far ultraviolet Spectroscopic Explorer (FUSE) had failed gyro during mission [22]. The study after the failure of FUSE uses hybrid integrated-rate parameters (IRP) – Euler filter approach.

$$\dot{D}(t) = \Omega(t) D(t) \tag{8}$$

where D(t) is the spacecraft attitude matrix. $\Omega(t) = -[\omega(t) \times]$, with $\omega(t)$ the spacecraft angular velocity and $[\omega(t) \times]$ defined as follows:

$$[\omega(t) \times] \triangleq \begin{bmatrix} 0 & -\omega_z & \omega_y \\ \omega_z & 0 & -\omega_x \\ -\omega_y & \omega_x & 0 \end{bmatrix} \tag{9}$$

The discrete-time version of the attitude matrix is:

$$D(k+1) = D[\theta(k+1) - \theta(k), \omega(k+1), \dot{\omega}(k+1), D(k)] \tag{10}$$

$$\theta(k) = [\theta_1(k)\theta_2(k)\theta_3(k)]^{\mathrm{T}} \qquad \theta_i(k) \triangleq \int_{t_0}^{t_k} \omega_i(\tau)d\tau \tag{11}$$

Chapter 6   MATLAB Simulation Results

The previous ADC team had achieved quite satisfying results with MATLAB simulation for both stabilization and attitude determination and maintenance phases. This year, the results were further improved.

6.1   Performance Improvement of the New Magnetorquer

Compare with last year, new magnetorquer was selected this year. Although more weight is added to the CubeSat and the structure group had to modify the layout of each component to fit them into the CubeSat, they have shown much better performance during stabilization phase.

Table 7: Comparison of Magnetorquers' Data

Model	MTO.2-1	MTO.5-1
Maximum moment	0.2 Am^2	0.5 Am^2
Max power	0.2W	0.3W

Using the same setting for the simulation from last year's ADC group, e.g. 5 degrees for yaw, pitch and roll angle and 5 degrees per second for initial angular velocity and the updated magnetorquer information, comparisons of the velocity profile and control output profile are shown below.
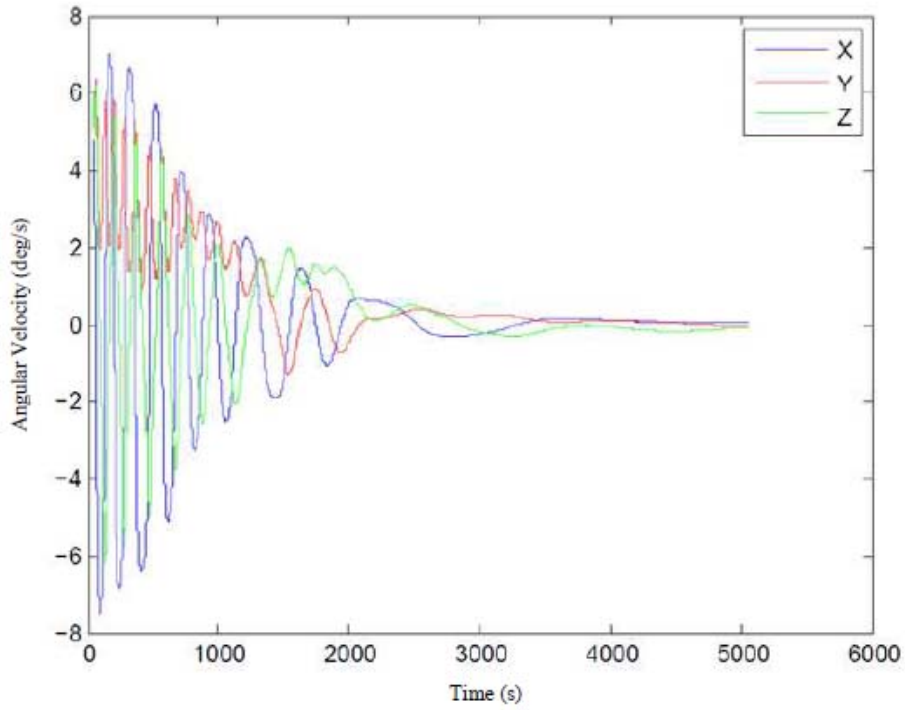
Figure 15: Figure 16: Angular velocity vs. Time from Previous Year
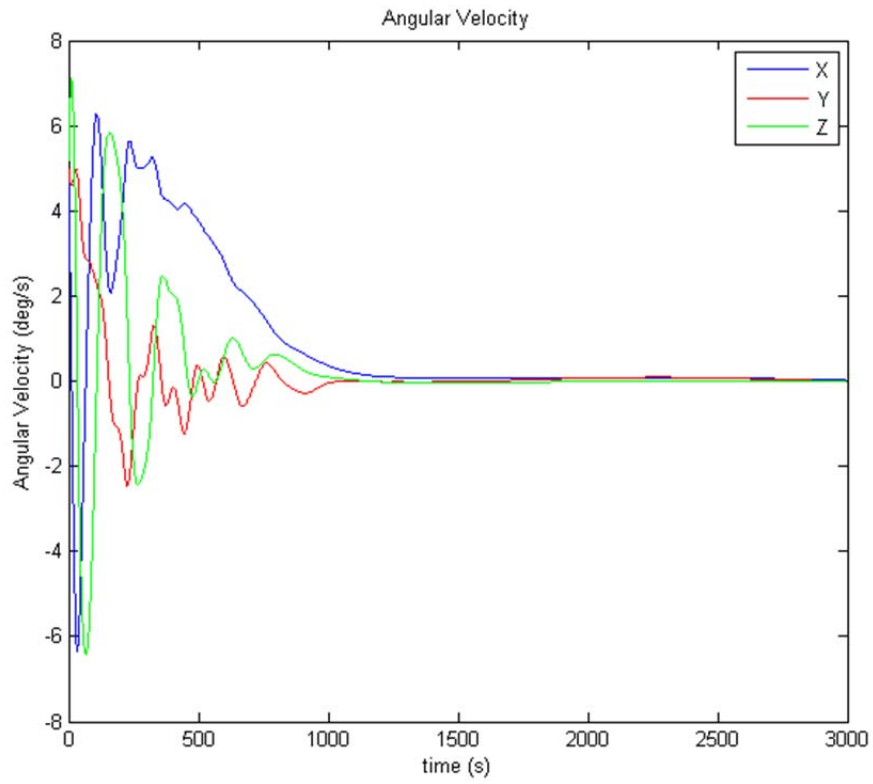
Figure 17: Figure 15: Angular velocity vs. Time from Current Result

33
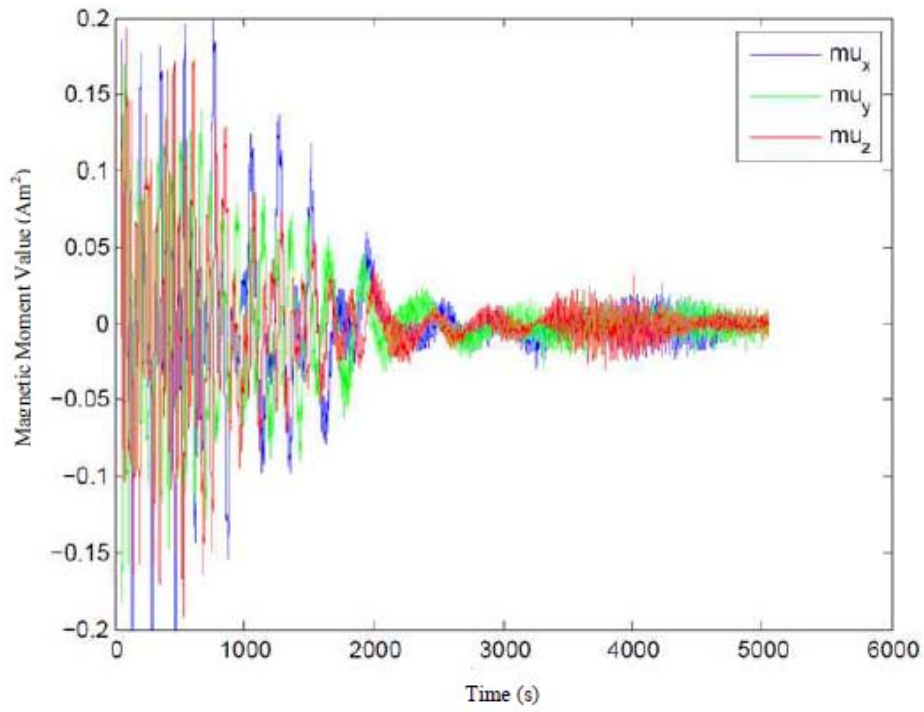
Figure 18: Magnetorquer Control Output vs. Time from previous year
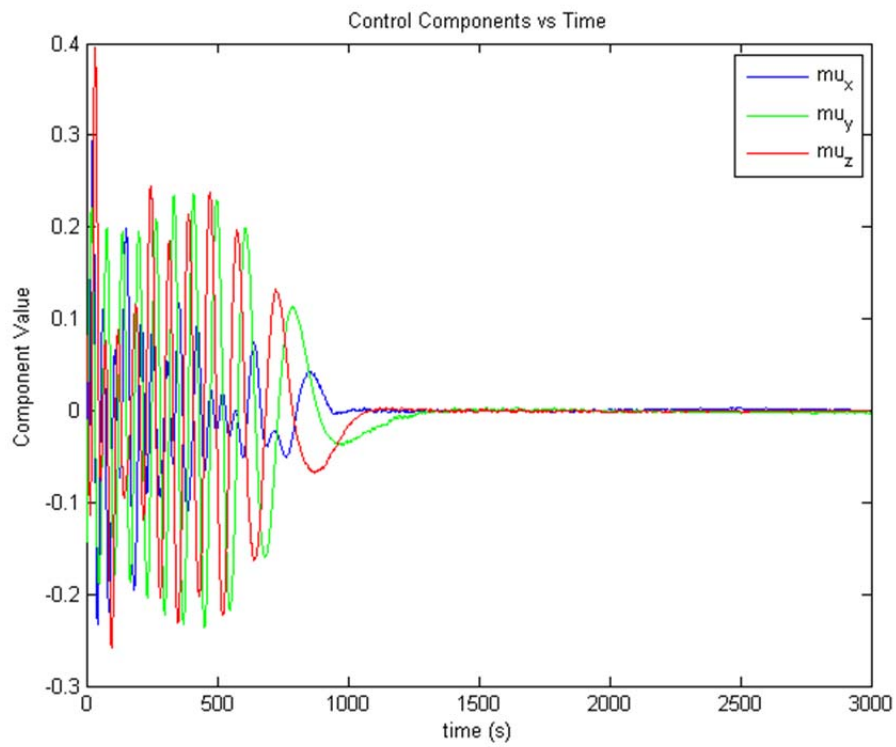
Figure 19: Magnetorquer Control Output vs. Time from current result

When the angular velocity for each components of the CubeSat is less than 0.1 degree per second, then it's considered that the satellite is stabilized. Using this criterion, the optimized stabilizing time from the last year was given to be around 3300 seconds whereas with the latest magnetorquer, the stabilizing time was much less and was estimated at about 1100 seconds. By analyzing the controller output, the reason why the new magnetorquer has such a huge improvement became obvious. The maximum moment produced by the new magnetorquer is 0.5 Am^2 which is twice more than that of 0.2 Am^2 of the old one. Also the plot from previous year showed that the old magnetorquers peak at the first 1000 seconds. As with the new magnetorquer, the output moment only went up to 0.4 Am^2 for the very first 100 seconds and went only slightly above 0.2 Am^2 after 100 seconds. The extra moment produced by the new magnetorquer had indeed improved the stabilizing time significantly.

6.2   De-tumbling Optimization

To further improve the performance of the control algorithm during stabilization period, the team decided to carry on with more investigations into the gain determination.

6.2.1   Optimized Single Fixed Gain Investigation

With the updated specifications for the new magnetorquer, updated de-tumbling time was acquired using the MATLAB simulation. Using 5 degrees for yaw, pitch and roll angle and 5 degrees per second for initial angular velocity, the summary of the de-tumbling time with different noise filters is shown below in the plot. EKF denotes extended Kalman filter, LPF denotes low pass filter and triad denotes the raw data without any filtering.
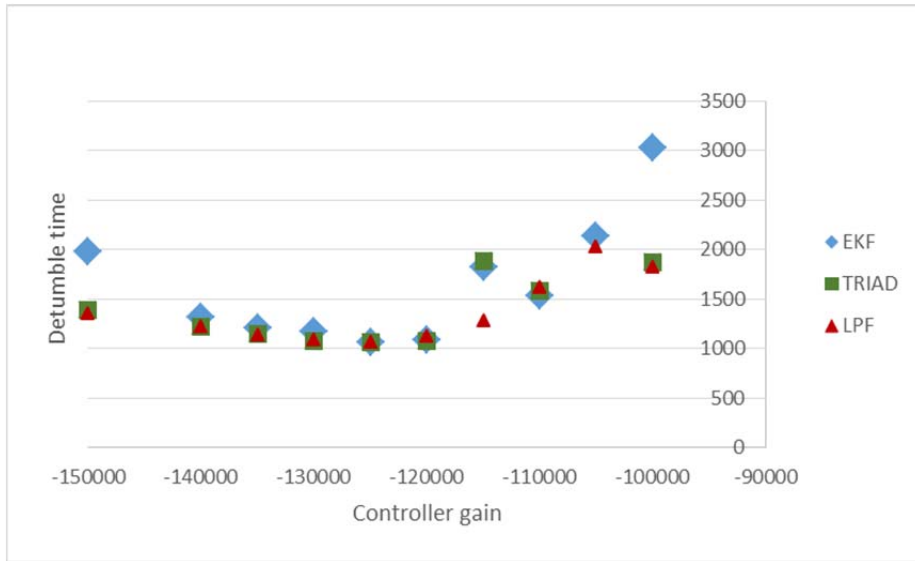
Figure 20: De-tumbling Time vs. Gain Value at Time Step of 0.5s
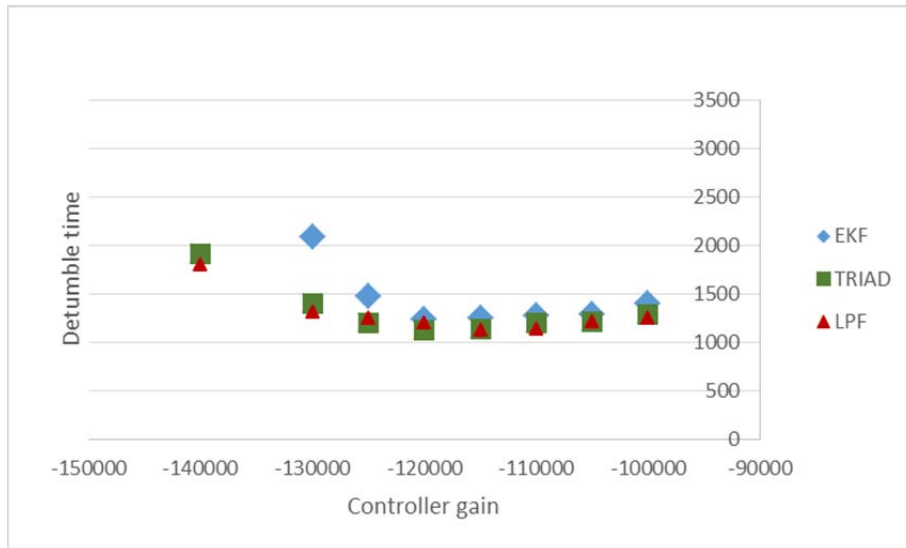
Figure 21: De-tumbling Time vs. Gain Value at Time Step of 5s

At time interval of 0.5 seconds, the optimized de-tumbling time of around 1100 seconds is observed at gain value of approximately -120000 to -125000. In the case of time interval of 5 seconds, the optimized de-tumbling time of around 1250 seconds is observed to be at gain value of approximately -115000 to -120000. The different results for different time interval revealed that if the sampling frequencies of the gyroscope and magnetorquer are high, better de-tumbling time was expected to be achieved and the magnetorquer can produce higher torque to control the satellite. If the sampling frequencies were low, the controller gain was relatively small because large gain will tend to overshoot

the system. In any cases, the gain cannot exceed certain values depending on the sampling frequency and further investigations of the critical value are needed for ensuring the system stability.

6.2.2 Introduction of multiple fixed gains and adaptive (state dependent) gain

Recall the equations for magnetorquer output and torque applied:

$$T = \mu \times B$$

$$\mu = -C \cdot (B \times \omega) \tag{12}$$

where μ is the controller output, B is the magnetic field vector, ω is the angular velocity vector and C is the controller gain.

The previous simulation was based merely on a single fixed value as controller gain. After further investigating, it is possible to improve the performance of the magnetorquer by implementing multiple fixed gain or adaptive gain. The cross product gave a vector and C was set to be a 3-by-3 matrix so to match the dimension of μ, the controller output as a vector.

As a multiple fixed gain, the controller gain C has the following form:

$$C = \begin{bmatrix} C_1 & 0 & 0 \\ 0 & C_2 & 0 \\ 0 & 0 & C_3 \end{bmatrix} \tag{13}$$

C_1, C_2 and C_3 have values on the order of 10^5 which are on the same order as the gain value for single fixed gain. For the simplicity of investigating the effects of implementing multiple fixed gains, C was taken to be a diagonal matrix. Instead of having single gain for all three axes, now each axis has its own gain value which means that output of each magnetorquer can be modified.

As for adaptive gain, the controller gain C has the following form:

$$C = \begin{bmatrix} f(B_i, \omega_i) & 0 & 0 \\ 0 & f(B_i, \omega_i) & 0 \\ 0 & 0 & f(B_i, \omega_i) \end{bmatrix} \quad i = x, y, z \tag{14}$$

$f(B_i, \omega_i)$ denotes that it is a function of all components of the magnetic field and angular velocity. Similarly, for the simplicity, C was also taken to be a diagonal matrix. The possible improvement by implementing adaptive gains was that at different strengths of magnetic field and angular velocities, the optimal controller gains would be different; therefore having adaptive gains can possibly improve the performance of the controller more.

6.3   Comparison of Three Gain Types

With the latest inertia matrix, along with the specifications of the new magnetorquer, MATLAB simulation results using single fixed gain, multiple fixed gains, and adaptive gain were obtained. However, the plots of angular velocity and controller output vs time are very similar and it's rather difficult to judge which gain mode is better. In order to study the differences among the three methods, the squares of the controller output are integrated over the same time period of 2500 seconds (note that controller output is directly proportional to the power consumption, it's reasonable to assume that the more controller outputs, the more energy it consumes) and below is the results of relative energy consumption by magnetorquer for each type of gains.

Table 8: De-tumbling Time and Energy Consumption with Three Different Gain Types

	Single fixed gain	Multiple fixed gains	Adaptive gain
x-axis [A.m^2]	9.1998	11.6167	6.7102
y-axis [A.m^2]	15.9138	11.4179	13.2193
z-axis [A.m^2]	10.4868	11.8592	13.7142
sum [A.m^2]	35.6003	34.8938	33.6437
De-tumble time [s]	1480	1340	1250

The total relative energy consumption for single fixed gain is the highest amongst all three, and three magnetorquers have uneven output, meaning the magnetorquer in y-axis does more work and leaving the other two in x- and z-axes do less work. In addition, the de-tumbling time using single fixed gain is the longest among all. Note that the de-tumbling time presented here is higher than the ones presented in the previous section of determination of optimal controller gain; the reason is inertia matrix has been updated since then and was used for the simulation results in this section.

The advantage of using multiple fixed gains is clearly seen that the total energy consumption is less, the de-tumbling time is less and more importantly each magnetorquer is able to provide similar amount of output so to achieve an even wear for the magnetorquers and reduce the possibility of breakdown during mission.

Lastly for the adaptive gain, both the energy consumption and the de-tumbling time are further reduced. The state depending function used for this simulation is:

$$C_1 = 19500(5 - \frac{B_y}{0.00005} - \frac{B_z}{0.00005} - \frac{\omega_y}{5} - \frac{\omega_z}{5})$$

(15)

The denominators in each term in function above were chosen relative to the maximum values of each component readings. B was on the order of maximum of 10^{-5} [Tesla] and ω was set initially to 5 degrees/s. This reasonable expression for the adaptive gain produces satisfying results. In order to achieve the even magnetorquer output, better de-tumbling time, and better energy consumption, further investigations are needed to find the best adaptive expressions for each entry. As in the simulation, controller gains are simplified to have only diagonal entries, replacing zeroes in the gain matrix could possibly improve the performance of the controller even more.

6.4 Attitude Maintenance

As desired by mission payload, the purpose of the CubeSat is to point to the sun as accurate as possible during lighting period. Last year has already achieved some results, but with the updated magnetorquer and inertia matrix information, additional investigation was needed. The algorithm which was already implemented in MATLAB simulation is quaternion feedback controller [1].

$$U = K_p\, q_e + K_d \omega \tag{16}$$

Proportional gain K_p, corrects the pointing error whereas derivative gain K_d corrects the angular velocity which tends to stabilize the system by applying torque opposite to the direction of rotation. So when the angular velocity is small, the term of proportional gain leads the magnetorquer output and when the angular velocity is high, the derivative gain will keep the magnetorquer output more for stabilization.

6.5 Results

After hundreds of hours of simulation run, the optimal gain was determined as follows:

Table 9: Gain Value for Attitude Maintenance

Gain Type	Value
Proportional gain	0.0003
Derivative gain	0.0004
Maximum derivative gain	0.006
Minimum derivative gain	0.0003
Derivative gain in eclipse	0.02

Because of the random errors produced in the MATLAB simulation, 10 simulation results were obtained and average of the sun pointing accuracy over time was taken and below is the plot:
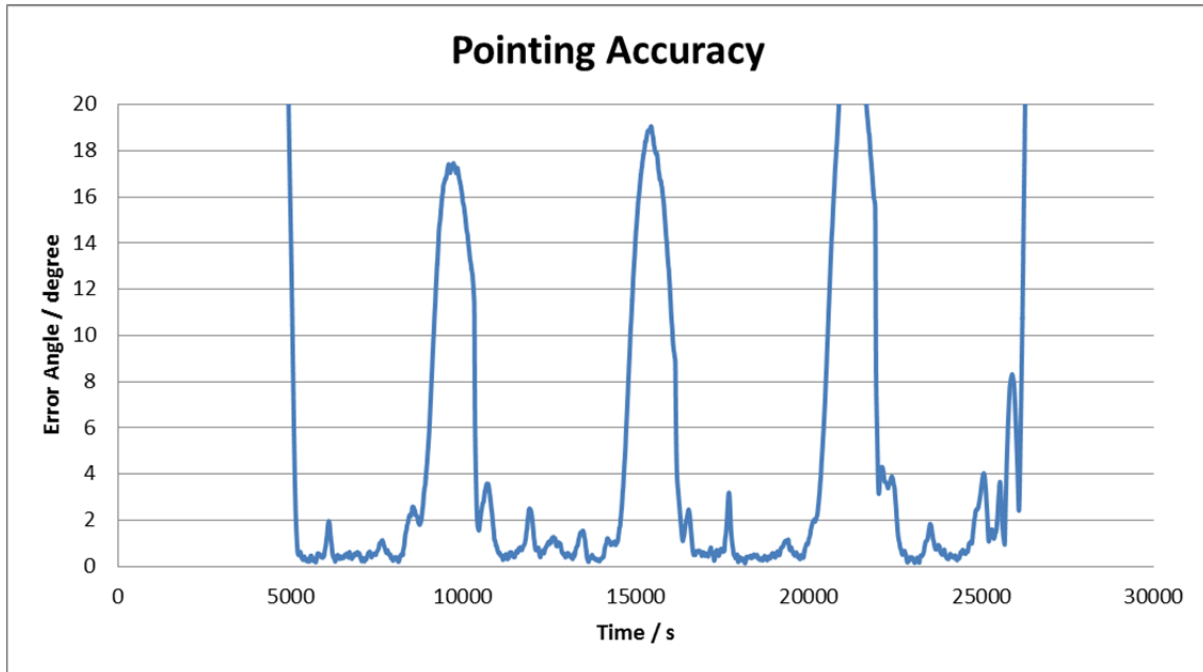
Figure 22: Pointing Accuracy vs time plot

Then the percentage of the sun pointing accuracy under certain degrees can be found. Note that the percentage was calculated out of the time during the sunny period which means the time spent by the CubeSat in eclipse period was omitted in the percentage calculation. A comparison of the sun pointing accuracy was also shown below.

Table 10: Sun Pointing Accuracy Comparison

Accuracy / degree	New Percentage	Percentage from last year
0.25	3.72%	5.21%
0.50	36.53%	15.14%
0.75	58.52%	30.95%
1.00	67.56%	44.47%
1.50	78.06%	62.70%
2.00	84.45%	72.09%
2.50	90.21%	
3.00	93.10%	

As seen from the table, the CubeSat now spends 12.3% more time within the 2 degree accuracy. And up to 93% within 3 degree accuracy. Although less time was spent within the 0.25 degree accuracy, the extra 20-30% more time within 1 degree is of the team's interest. The improvement of the pointing accuracy could be resulted from few changes that were made: the change of the inertia matrix, new magnetorquer and simpler sun sensor algorithm.
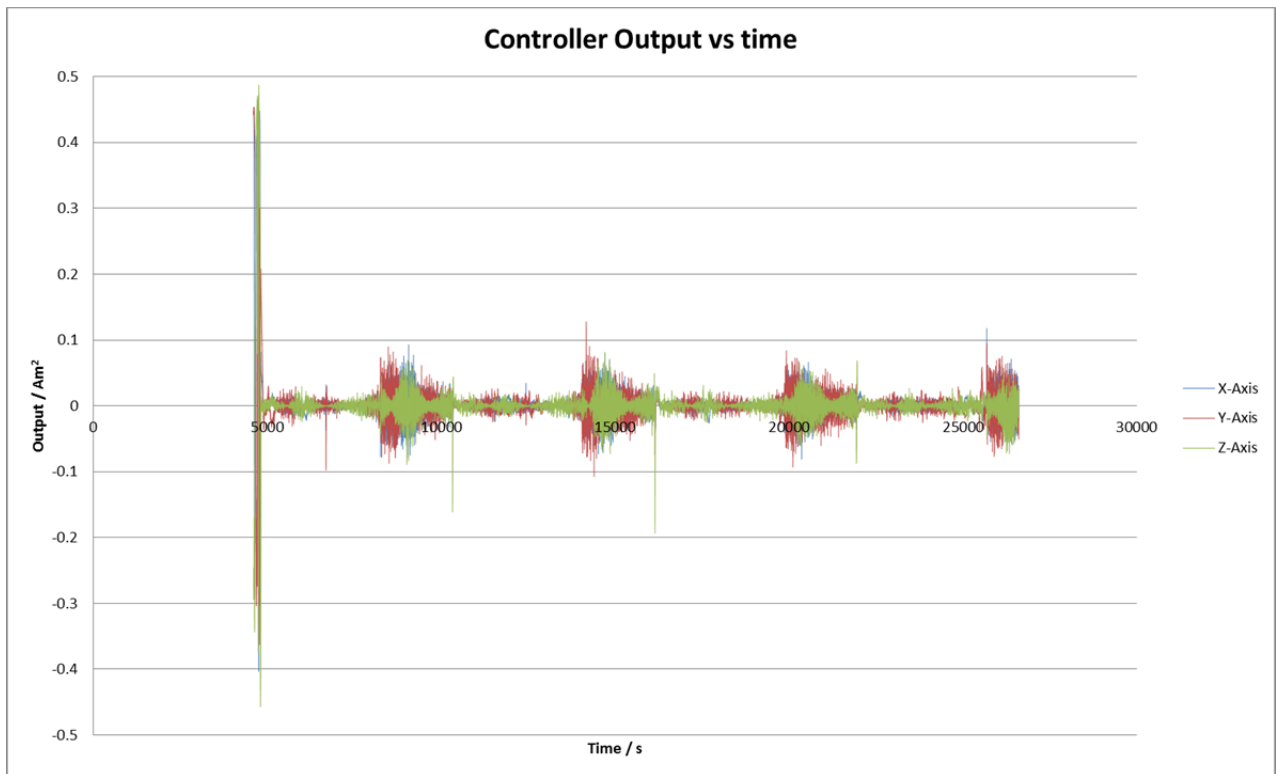
Figure 23: Controller output during Attitude Maintenance

From the figure of magnetorquer output, it can be seen that the controller peaks at its limit, but it's only for the first few hundreds seconds. The new magnetorquer produced extra power to control the CubeSat, and reduced the time to achieve its desired pointing angle more quickly. But when it came to minor maneuverer for pointing corrections, the new magnetorquers had no advantages over the old and less powerful ones. What the new magnetorquer can achieve was to shorten the time for the CubeSat to

turn so that the fine sun sensor can obtain steady readings and achieve a small gain in the point

percentages for one sunny period. However as for the whole mission, the extra time spent in sight of the

Sun would be amplified in hours and gave the payload instrument more accurate readings.

Chapter 7   ADC Test Bed

7.1   Tabletop Test Bed
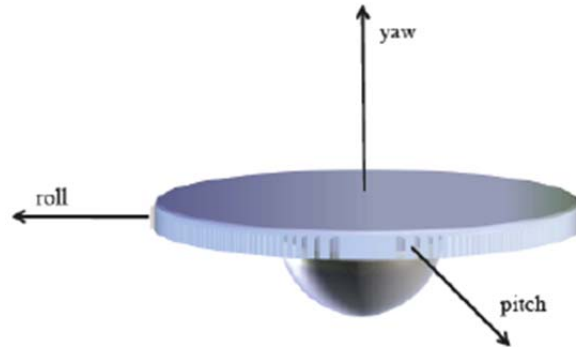
Figure 24: Visualization of Tabletop Test Bed

The purpose of the test bed is to prove that our Attitude Determination and control system simulation works using magnetorquers, gyroscope, and on board computer. The rotational air bearing can rotate up to fifty degrees off nominal in both the pitch and roll axes and support up to eighty kilograms. The air bearing has three orthogonal reaction wheels for attitude control and three orthogonal torque coils for reaction wheel desaturation or attitude control. The testbed uses inertial measurement units and built in-house sun and Earth sensors for attitude estimation. The testbed communicates wirelessly with a nearby ground station computer for reprogramming and data storage. The air bearing has manual as well as automatic center of mass adjustment devices used to reduce torque due to gravity on the system

The primary objective of the air bearing structure is to provide a physical platform capable of interfacing with the hemispherical base as well as provide attachment points and stability for the components necessary to perform ADCS testing [23]. The foundation of the structure is the hemisphere that oats on the cushion of compressed air. The hemisphere is the only portion of the vehicle that is in contact with the fixed inertial air bearing support column.

The hemisphere, however, is not actually touching the support column, but rather slightly above the column supported completely by a layer of compressed air. This support method is what gives the air bearing the ability to rotate in all three axes with significantly reduced friction while also being constrained to zero translational motion.

Figure 25: Air-Bearing Shape

The air bearing that supports the platform is located on top of a pedestal structure (12 in high) and it allows the platform to move without friction 45 deg about the two horizontal axes (x and y) and 360deg about the vertical (z) axis. The bearing is the SRA250 spherical air bearing designed and manufactured by Specialty Components Inc. The bearing itself is made of 600 aluminum and can hold up to 748 lbf of load when operating at 80 psi air pressure. The GIT platform bearing is operated at 30 psi which corresponds to approximately 300 lbf of vertical load.

The aluminum platform provides a mounting surface for the several simulator subsystems. The location of the center of mass (desired to be at the center of rotation of the simulator – in this case the center of the bearing rotor) can be changed by positioning different counterweights in various slots and holes located at several places on the platform. Care has been taken to position all major components of the simulator, such as momentum wheels, batteries, amplifiers, etc. in a symmetric fashion. This makes it easy to balance the platform as well as locate the principal axes [24].

Specialty Components were able to provide us a drawing of the SRA250 spherical air bearing in order to make sure that our testbed design will be able to carry the SRA250 and match with our dimensions.
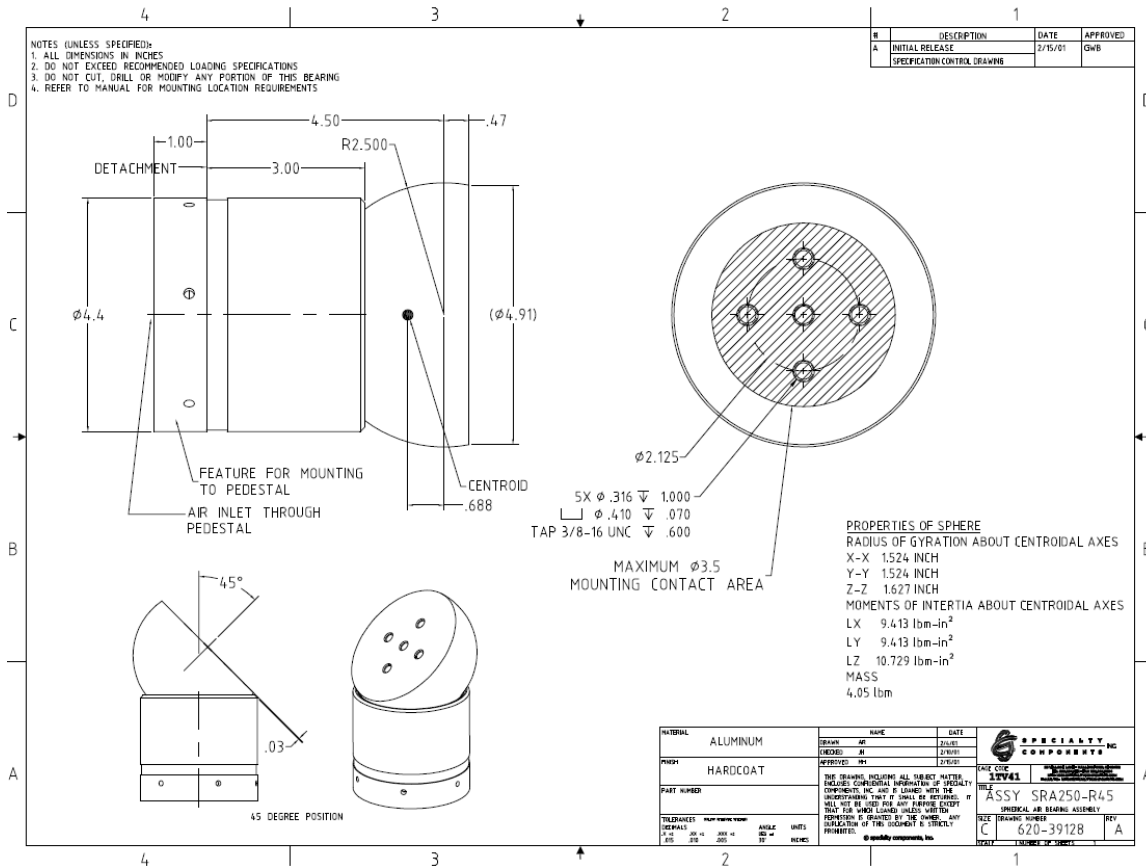
Figure 26: Specialty Components SRA250 drawing

As a backup plan in case we won't be able to by the SRA250 from Specialty Components, we contacted another air bearing company located in NH called Nelson Air Corp and requested the drawing for their spherical air bearing. Then, we compared both dimensions and re-dimensioned the testbed on SolidWorks to make sure whichever air bearing the next year team decides to go with it will be able to be mounted on this specific testbed.
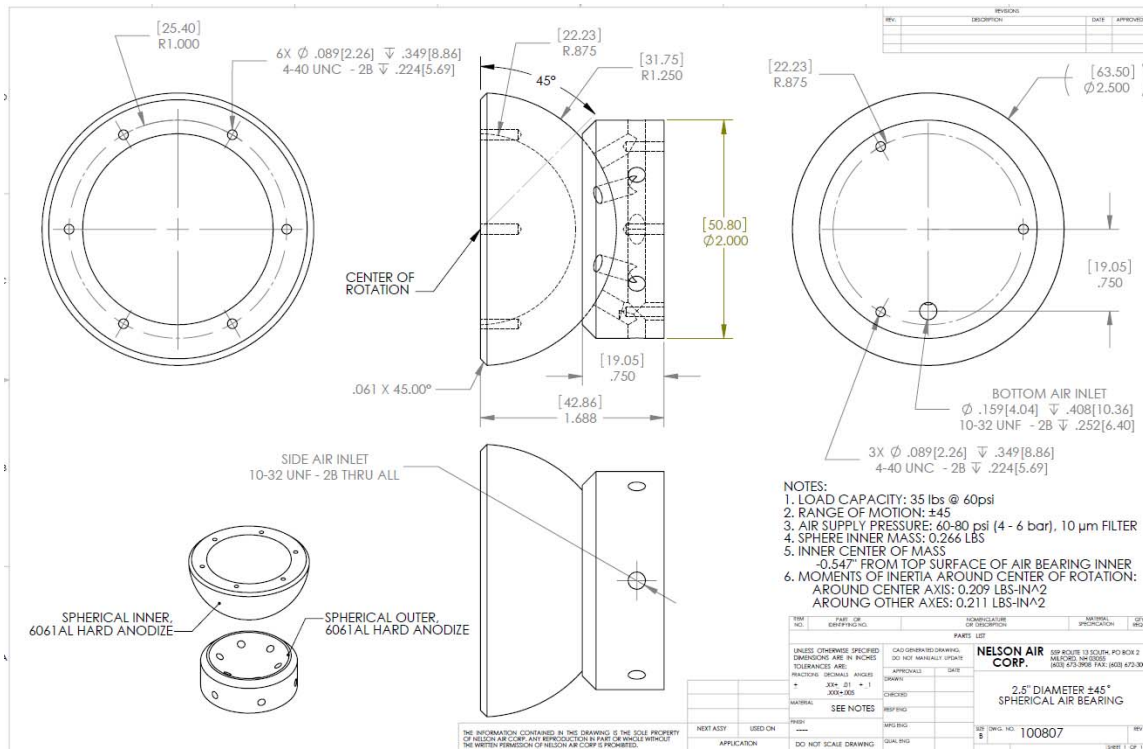
Figure 27: Nelson Air Corp Air Bearing drawing

Due to the small flying heights typical of air bearings, external gas pressure sources must be free of contaminants in order to allow proper operation.

Incoming air/gas should be conditioned to the following:

- Absolute filtration of particles to 1 microns

- Relative humidity less than 85% (non-condensing)

- No oils/ resins/ wax (coalescing / charcoal filter)

System designs should include provisions to prevent accidental motion of the bearing without adequate pressure. Pressure Interlocks and/or locking mechanisms with hard stops are prudent additions to mechanisms which use air bearings.

Figure 28: Air Quality Requirements

7.2   Test Bed Design:
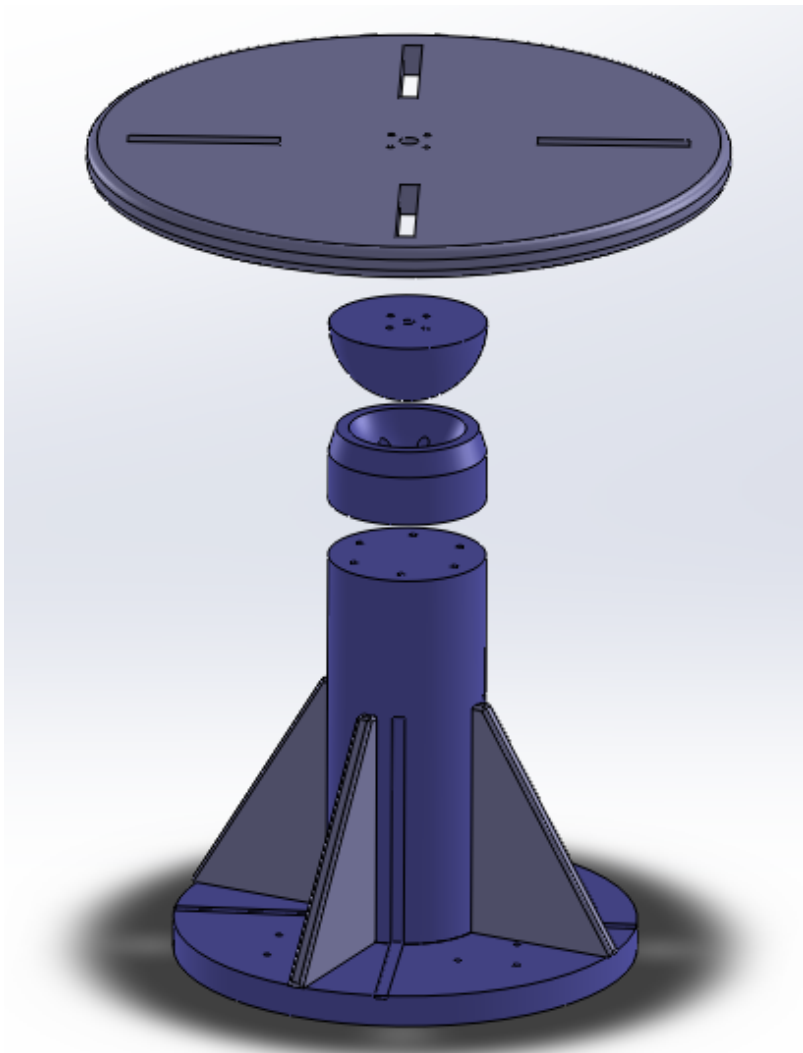
Figure 29: Test Bed Design

Cylindrical Stand:	Side Support:	Bottom Disk (Stand)
• 5 in diameter	5 in horizontal distance	15 in diameter
• 12 in height	7.5 in height	1 in thickness
• 1045 Carbon Steel	0.5 in thickness	Hot-Rolled Alloy Steel
	1018 Carbon Steel	

7.3   Stress & Displacement Analysis:

Stress Analysis Characteristics:

M = 6 [Kg]

Ftotal = 60 [N]

F / Peace = 15 [N]

7.3.1   Tabletop Disk (Aluminum):

Yield Strength = 27,574,200 [N/m^2]
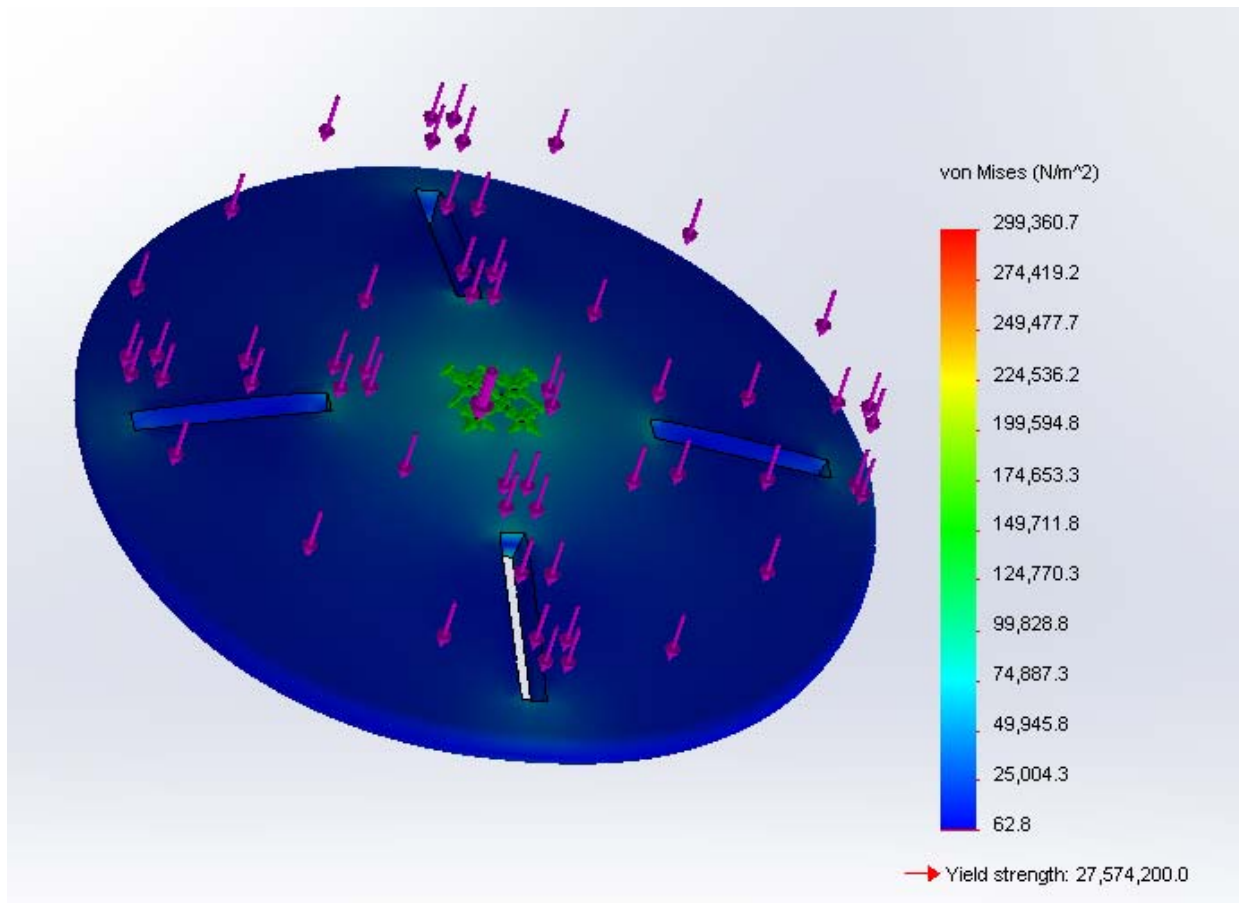
Figure 30: Tabletop Disk Strength Analysis

Max Displacement = 8.784e-004 [mm]
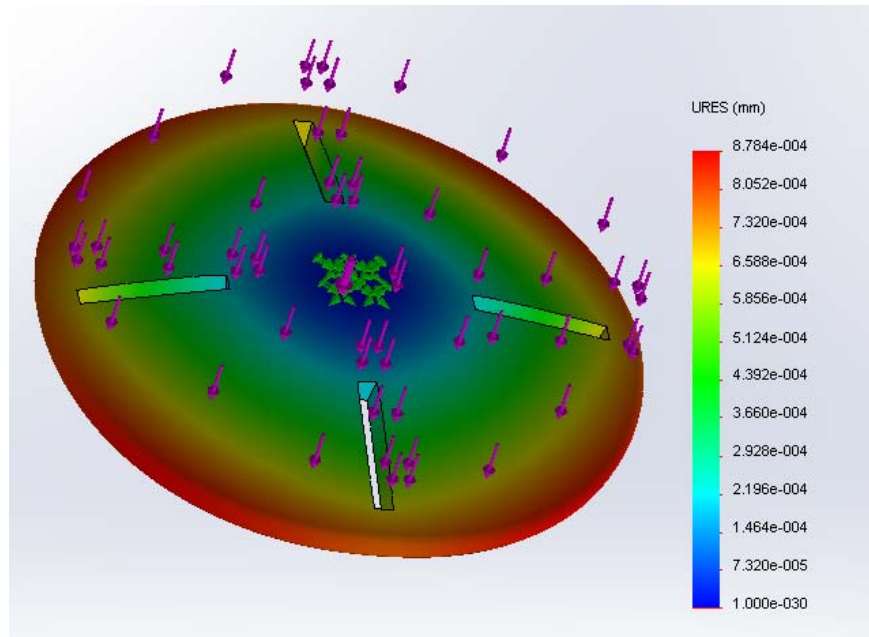
Figure 31: Tabletop Disk Displacement

7.3.2 Air Bearing Stand (1045 Carbon Steel):

Max Displacement = 2.517e-006 [mm]
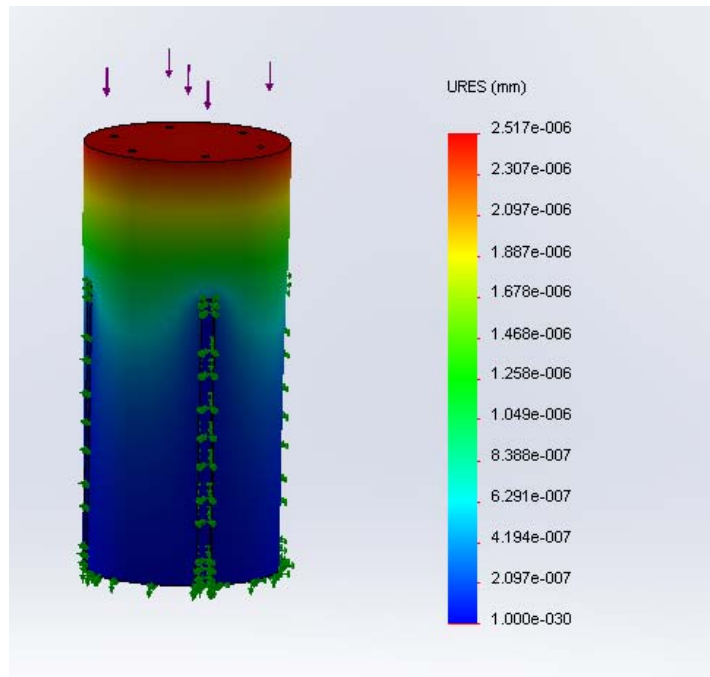
Figure 32: Air Bearing Stand Displacement Analysis

Yield Strength = 620,422,016 [N/m^2]
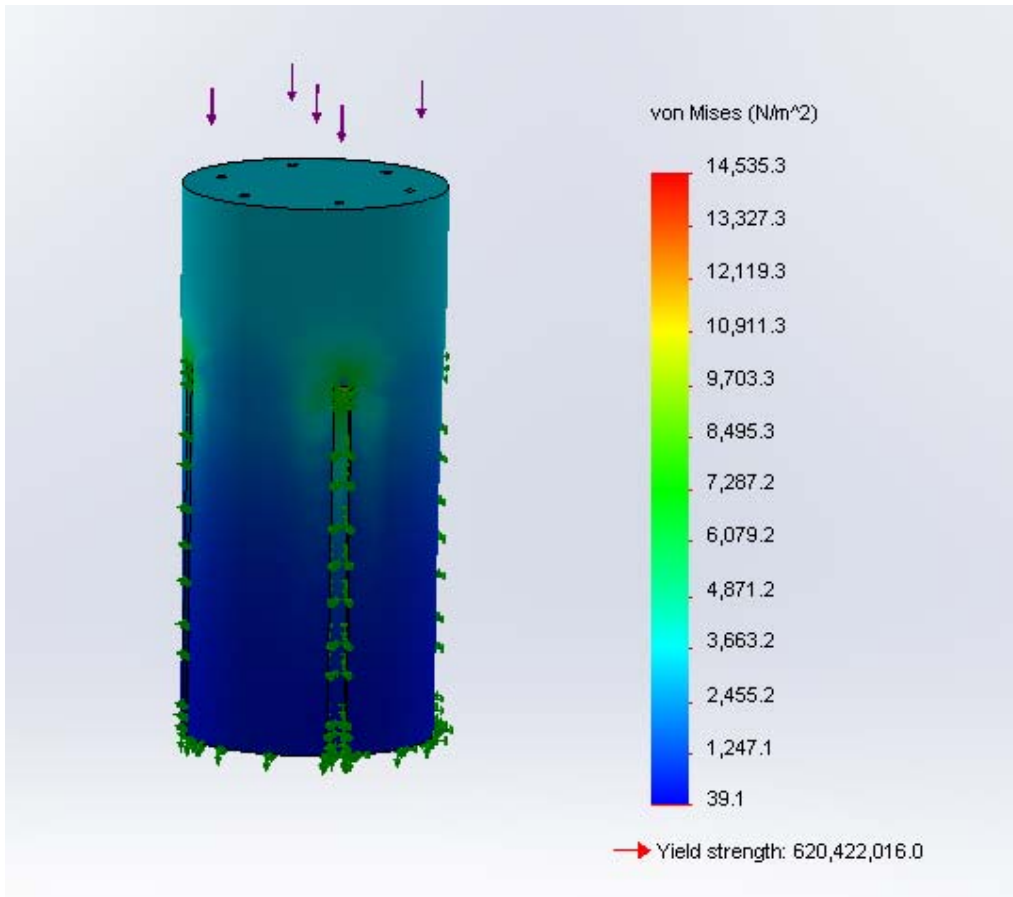
Figure 33: Air Bearing Stand Strength Analysis

7.4 Test Bed Material Selection

The updated test bed design for this year required materials to be selected for three key features of the test bed stand. The parts of the test bed design that were selected to be constructed this year were the baseplate, the support fins, and the central cylinder. Once these pieces are put together, a future team could outline a test bed experimental section and table-top design that fits to the support stand that will be constructed this year. Leaving the open-ended design seems to be the best idea, as it gives future teams a starting point when they begin to design an experimental set up for a test bed. After urging from the mechanical department, MSC Industrial Direct products were selected as the best options due to the array of products available, pricing, and quality of the products, as well as discounts the university may be able to arrange with the company itself.

7.4.1 Central Cylinder

Figure 34: The 1045 Carbon High Strength Steel Rod

Possibly the most important part of the test bed design is the central cylinder that supports the air bearing and the rest of the tabletop test bed. This part needs to be able to withstand the stresses and displacements outlined above. The highest quality steel available in the required dimensions is the 1045 High Strength Cold Finished Steel, made conveniently in the 5'' diameter by 12'' size that our test bed

design outlines. The machining of this product will be the most time consuming and delicate. The higher quality of the steel requires greater care and more practiced machining techniques. This piece will have slats machined into the side at the 4 places where the support fins attach to the side. The slats will be 0.5'' to have the fins slide in before they are welded to the cylinder. The bottom of the cylinder will have screw holes machined into it to allow screws to attach from the optical table, through the baseplate, to the cylinder. The top of the cylinder will have holes machined to allow the future attachment of a spherical air bearing, upon which the experiment portion of the test bed will sit.

7.4.2   Support Fins

Figure 35: The 1018 Carbon Steel Sheet

The fins used to support the main cylinder are necessary to reduce the stresses on the cylinder and make the overall test bed much more stable. The quality of the material used in the construction of these fins does not, however, need to be as high as the material used in the cylinder. The material selected is 1018 Cold Finished Steel. This product is a highly used product in industry, and holds all of the characteristics that the test bed design outlines. This product will be purchased in 1 sheet, with the required thickness of 0.5''. That sheet will then be cut into the four different 5'' by 7.5'' triangular support fins. This product has the least amount of machining required, as it is simply being cut. These fins

will be inserted into the slats of the cylinder and baseplate, and welded as well to the cylinder and

baseplate.

7.4.3   Test Bed Baseplate

Figure 36: The Alloy Steel Hot-Rolled Steel Plate

The baseplate of the test bed design will need to be solid enough to support all of the normal

stresses caused by the test bed in motion, as well as need to be able to be machined. The most important

characteristic for the baseplate will be its ability to be machined to the required dimensions and still

provide the support that the test bed calls for. The baseplate will have many holes machined into it, for

fixing the cylinder to the baseplate, as well as fixing the baseplate to the optical table on which the whole

test bed is mounted. The baseplate will also have four slats machined into its top surface to allow the four

support fins to slide into before they are welded together. The slats will be 0.5'' wide, and 5'' in length

from the outer diameter of the baseplate towards the center of the test bed.

7.5   Test Bed Configuration

The Attitude Determination and Control project from last year suggested a less robust, and thus cheaper, design for the components and actuators of the test bed. The aluminum board affixed at the top of the test bed design will be the surface to which all test bed components are attached. These components include control computer processors, data handling transmitter/receiver boards, sensors for acquisition, and actuators for motion control.

The configuration and alignment of these items is crucial as the main goal of the test bed is to balance its own center of rotation with its center of balance. Last year's team researched designs of successful test beds and suggested taking a similar approach, with a few cutbacks taken where they could be to reduce the overall cost of creating this test bed. All of the components suggested below have been used by either the Naval Post-Graduate Test Bed, or by the Journal of Applied Research and Technology schematic posted in the IEEE publication.

7.5.1   Central Processing Unit

Figure 37:ADL LX8PC-AMD Geode LX800 Single Board Computer

The overall goal of the test bed is to produce stable results using the type of actuators that are going to be used on the CubeSat while controlling them with the algorithms designed to control the CubeSat.

The test bed itself will be attempting to directly mimic the control policies that are going to be implemented within the CubeSat. The main processor of the test bed will need to be able to command the

data from all of the sensors, motors, and other processors and control the system to a stable plane of motion.

The Advanced Digital Logic LX8PC-AMD Geode LX800 Single Board Computer has been selected to run the test bed for three main characteristics. It has the capability to run at the speeds that the CubeSat's ADCS board runs at, allowing us to prove that control of a system similar to our design for the CubeSat can be handled through the ADCS board sub-computer, which is being imitated by this processor in the test bed design. It is stackable in the PC/104 format, allowing easier integration into the design of the test bed, and the part is scalable in price, allowing, if possible, a less robust design, reducing the budget [17].

This component will also function as the power management system for the test bed. The power supply will be connected with a serial +5V direct current connection, as well as with all power pins of the PC/104 configuration for power management. The PC/104 format connector is shown below.
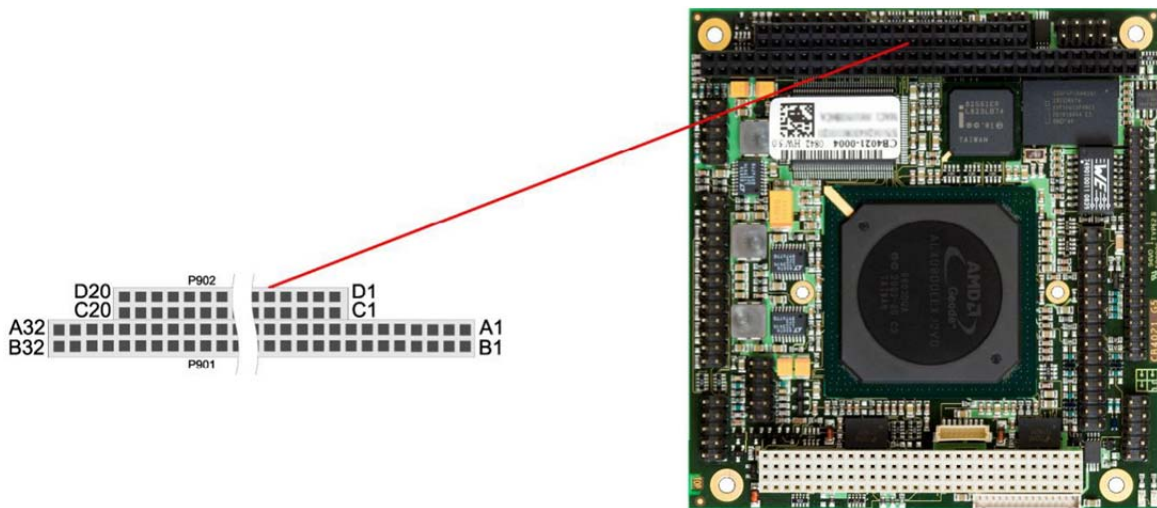
Figure 38: PC/104 Location for SBC

7.5.2 Wireless Communication Board
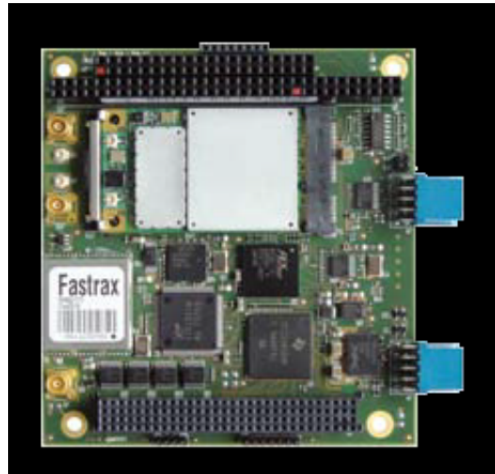
Figure 39: Eurotech COM-1480 Wireless Communication Board

The design of the test bed calls for a balance of the components on the spherical air bearing. To avoid the complicity of the wiring to all of the computer components from our data acquisition system, wireless communication will be used. A single Eurotech COM-1480 is needed to carry out this task. The board is PC/104 compatible, allowing the board to be easily integrated into the system with the Single Board Computer and the power supply. This is ideal because the weight of the board will be distributed evenly with the rest of the components, making it easier to balance the entire system. An outline of the system is shown below. Further analysis will need to be done on this product to find a good, and yet cheap, receiver for this system [25].

7.5.3 On-Board Communication Board

Figure 40: Accesio 104-COM-8SM Communication Board

The board selected for on board communication will need to be able to do two things. First, this component needed to connect easily both electrically and physically to the computer systems selected for processing. This is achieved by the 104-COM-8SM's PC/104 Bus connectivity. Second, the serial connections of this board needed to be compatible with the systems sending it information. These systems would be the motors controlling the balance of the system. The motors for the test bed have not been selected due to the unknown strength of the magnetorquers, which the motors need to be on par with [26].

7.5.4 I/O Transceiver Board

Figure 41: Diamond-MM-32-AT I/O Transceiver Board

The actuators of the test bed (the magnetorquers, yet to be selected) will need to be interfaced with the control program through an Input/output controller. This board allows the computer system to easily control the actuators. Connection from this board to the computer is carried out through the PC/104 Bus. The Diamond-MM-32-AT is compatible with many different types of analog and digital inputs, allowing it to be a good choice for the control of the yet unknown actuators [27].

7.6 Power Considerations

The table below shows the power required for each component highlighted. As it can be seen, the components all connect to the power source with a +5V direct current connection (DC).

Table 11: Component Power Information

Type	Power (mA)	Voltage (V)
LX8PC-AMD Geode LX800	1480	+5 (DC)
Eurotech COM-1480	900	+5 (DC)
Accesio 104-COM-8SM	80	+5 (DC)
Diamond-MM-32-AT I/O	410	+5 (DC)

7.6.1 Battery

Figure 42: Inspired Energy ND2054 Smart Li Ion Battery

The main consideration for the battery was its ability to supply the power required evenly to the systems. The ND2054 series of batteries from Inspired Energy provide a scalable option for power supply. The ND2054 is rated to function at levels acceptable for our theorized test bed specifications, and has been used by the Naval Post-Graduate Test Bed design. Another benefit of the ND2054 series is the mass. It weighs in at just less than 0.25 kg, which keeps the overall mass of the components well below the cap of 6 kg. The possibility of needing more than one battery exists, as the power requirements for the motors and magnetorquers could be greater than that provided by one battery. This is not necessarily a drawback, as the use of multiple batteries could allow easier balancing of the overall system, simplifying the computations necessary.

Chapter 8 Conclusion & Recommendations

This project increased the effectiveness of the MATLAB control code, as the total time within the required pointing increased by about 12.5% [1]. The use of a stronger magnetic torquer allowed the control algorithm to better de-tumble the CubeSat, as the stronger magnetic moment provided by the bigger torquer turns the spacecraft body much faster. The updated inertial matrix provided by the Structural and Mission Analysis team was not as idealized as the previous estimate, but nonetheless still allowed full attitude control using our specified policies. Also, a theorized set up for a test bed has been developed, and materials selected for the planned construction of the test bed stand.

8.1   Test Bed Material Purchasing

With materials outlined as above, the decision was made for this project to suggest specific parts and have a succinct set of parts to order available for future WPI CubeSat teams. Originally parts were selected from the online McMaster-Carr order guide. However, after urging from the mechanical department, MSC Industrial Direct parts should be purchased for use in the test bed design.

8.2   Attitude Simulation

The new 4+1 sun sensor setting and the nature of one-axis readings from the coarse sun sensors have limited the readings from the sensors. As in simulation section, algorithm for sun sensor was tested and approved to be effective in the overall control system; however, the current method of obtaining sun sensor readings can be improved using complicated algorithm integrate the sun sensors and gyroscope and achieve more accurate sun position estimation. The advantage of acquiring more accurate sun position is avoiding controller overshoot the system too much which could lead to save the time for initial attitude determination. But associated disadvantage by using complicated algorithm is that it consumes more computing power. This is one aspect of what the future work would be.

Also as of future interest, the expressions for the gain selection in stabilization phase can be investigated further to find improve the control algorithms. From previous section, system with adaptive gains produced better results. As for the computing power consumed by calculating the adaptive gains, depending on the selection of the expressions, for the current selection the power used is minor compare with other calculations. So for the improvement of the stabilization phase, adaptive gains should be investigated and determined.

Chapter 9   References

[1]   N. N. &. D. V. Elizabeth Dawson, "Attittude Determination and Control System Design For A CubeSat Mission," WPI , Worcester, 2012.

[2]   D. V. Guerrant, "Desing and Analysis of Fully Magnetic Control for Picosatellite Stabilization," San Luis Obispo, 2005.

[3]   P. W. Steyn, "Magnetic Attitude Determination and Control for Low Earth Orbiting Small Satellites," Matieland.

[4]   Y. Yang, "Quaternion Based Model for Momentum Biased Nadir Pointing Spacecraft," *Aerospace Science and Technology,* pp. 199-202, 2010.

[5]   M. B. A. B. Y. H. M. S. A.M. Si Mohammed, "Simulation of microsatellite attitude using Kalman filtering in orbit results," *Simulation Modelling Practice and Theory,* pp. 257-277, 2008.

[6]   G. W. a. G. Bishop, "An Introduction to the Kalman Filter," University of North Carolina at Chapel Hill, Chapel Hill, NC, 2006.

[7]   M. I. Ribeiro, "Kalman and Extended Kalman Filters: Concept, Derivation and Properties," 2004.

[8]   N. K. Y. B. K. a. G. I. Ure, "The Development of a Software and Hardware-in-the-Loop Test System for ITU-PSAT II Nano Satellite ADCS," *IEEE,* pp. 1-15, 2011.

[9]   K. A. KOPECKY, "Numerical Differentiation," 2007.

[10]   H. F. &. E. P. Simoncelli, "Differentiation of discrete multi-dimensional signal," *IEEE Transactions on image processing.*

[11]   "Coarse Sun sensor data sheet," Aeosatro, [Online]. Available: http://www.aeroastro.com/uploads/data%20sheets/Coarse%20Sun%20Sensor%20Data %20Sheet.pdf.

[12]   "CubeSat Sun Sensor," SSBV, [Online]. Available: http://www.ssbv.com/ProductDatasheets/page39/page29/index.html.

[13]   "ADXRS450Z Evaluation Board," Analog Devices, [Online]. Available: http://www.analog.com/en/mems-sensors/mems-gyroscopes/adxrs450/products/EVAL-ADXRS450Z/eb.html.

[14]   "Gyroscope," Gyroscope.org, [Online]. Available: http://www.gyroscopes.org/index.asp.

[15]   T. Bak, "Spacecraft Attitude Determination - a Magnetometer Approach," Aalborg, 1999.

[16]   "Triple Axis Magnetometer Breakout," Sparfun Electronics, [Online]. Available: https://www.sparkfun.com/products/10530.

[17]   "Single Board Computer," Embedded Solution, [Online]. Available: http://www.adl-usa.com/products/cpu/datapage.php?pid=ADLLX8PC.

[18]   "High Definition Geomagnetic Model," NOAA, [Online]. Available:

http://www.ngdc.noaa.gov/geomag/hdgm.shtml.

[19]   "International Geomagnetic Reference Field: the eleventh generation," US Department of Commerce, 2010.

[20]   e. Stefan Maus, "The US/UK World Magnetic Model for 2010-2015," NOAA, Boulder, 2010.

[21]   J. D. a. D. F. B. G. A. Natanson and M. S. Challa, "Magnetometer-Only Attitude and Rate Determination for a Gyro-Less Spacecraft," National Aeronautics and Space Administration, Greenbelt, Maryland.

[22]   J. T. a. Y. O. Rick Harman, "GYROLESS ATTITUDE AND RATE ESTIMATION GYROLESS ATTITUDE AND RATE ESTIMATION".

[23]   D. Meissner, "A three degree of freedom test bed for nanosatellite and cubesat attitude dynamics, determination, and control," Naval Postgraduate School, 2009.

[24]   P. D. W. M. Corey Whitcomb Crowell, "Development and Analysis of a Small Satellite Attitude Determination and Control System Testbed," Boston, 2011.

[25]   "COM-1480," Eurotech, [Online]. Available: http://www.eurotech.com/en/products/COM-1480.

[26]   "104-COM-8SM Family," [Online]. Available: http://accesio.com/go.cgi?p=../104/104-com-8sm.html.

[27]   "Diamond-MM-32-AT," Diamond Systems, [Online]. Available: http://www.diamondsystems.com/products/diamondmm32at.

[28]   J. Prado, "Three-axis air bearing based platform for small satellite attitude determination and control simulations," *IEEE,* 2003.

[29]   Hewlett-Packard Corporation, "Advanced Configuration and Power Interface Specification, Revision 2.0," 2000.

[30]   "TNO coarse sun sensor," ESA, [Online]. Available: http://telecom.esa.int/telecom/www/object/index.cfm?fobjectid=28404.

[31]   "Wilkinson Microwave Anistropy Probe: Explanatory supplement," NASA, 2003.

[32]   "Freescale semiconductor," [Online]. Available: http://cache.freescale.com/files/sensors/doc/data_sheet/FXOS8700CQ.pdf?fpsp=1.

[33]   "CubeSat Attitude Determination and Control Systems," Clyde Space, [Online]. Available: http://www.clyde-space.com/cubesat_shop/adcs.

[34]   "CubeSat Sun Sensor," CubeSatshop, [Online]. Available: http://www.cubesatshop.com/index.php?page=shop.product_details&product_id=104&flypage=flypage.tpl&pop=0&option=com_virtuemart&Itemid=65&vmcchk=1&Itemid=65.

[35]   "Numerical Differentiation," [Online]. Available: http://elm.eeng.dcu.ie/~ee317/Course_Notes/handout1.pdf.

[36]   "3-Axis Digital Compass IC," Honeywell, [Online]. Available: http://dlnmh9ip6v2uc.cloudfront.net/datasheets/Sensors/Magneto/HMC5883L-FDS.pdf.

[37]   T. H. K. Z.-H. Tian Xiang, "Design and On-orbit Performance of the Attitude Determination and Control System for the ZDPS-1A Pico-Satellite," *Acta Astronautica,* pp.

182-196, 2011.

[38]   W. M. A. R. F. B. Thomas W. Flatley, "A B-Dot Acquisition Controller for the RADARSAT Spacecraft," Goddard Space Flight Center, Greenbelt, Maryland.

[39]   D. P. V. Paul Tisa, "Performance Analysis of Control Algorithms for FalconSat-3," *American Astronautical Society,* p. 18, 2006.

[40]   M. L. P. a. Y. Oshman, "Spacecraft Attitude Rate Estimation From Geomagnetic Field Measurements".

[41]   F. L. Markley, "Attitude Determination Using Vector Observations and The singular Value Decomposition," *The Journal of the Astronautical Sciences,* pp. 245-258, 1988.

[42]   J. M. E. M. Awais Abbas, "ATTITUDE DETERMINATION AND CONTROL SUB-SYSTEM SATELLITE CONTROLLER," *IEEE,* p. 6, 2011.

[43]   L. S. Li Da, "Real -Time Sequential Kalman Filter Sensor Registration Algorithm," *IEEE,* 2006.

[44]   E. G. L. John L. Crassidis, "ATTITUDE DETERMINATION USING COMBINED GPS AND THREE-AXIS MAGNETOMETER DATA".

[45]   M. I. G. A.-. W. B. Group, "Annex 1 Net FDI Inflows, 2000-2008," MIGA, Washington, 2009.

[46]   B. J. a. B. Carpenter, "Optimal Placement of Spacecraft Sun Sensors Using Stochastic Optimization," in *IEEE Aerospace* , 2004.

[47]   J. M. G. Aage Skullestad, "H Control of a Gravity Gradient Stabilized Satelite," *Control Engineering Practice,* pp. 975-983, 2000.

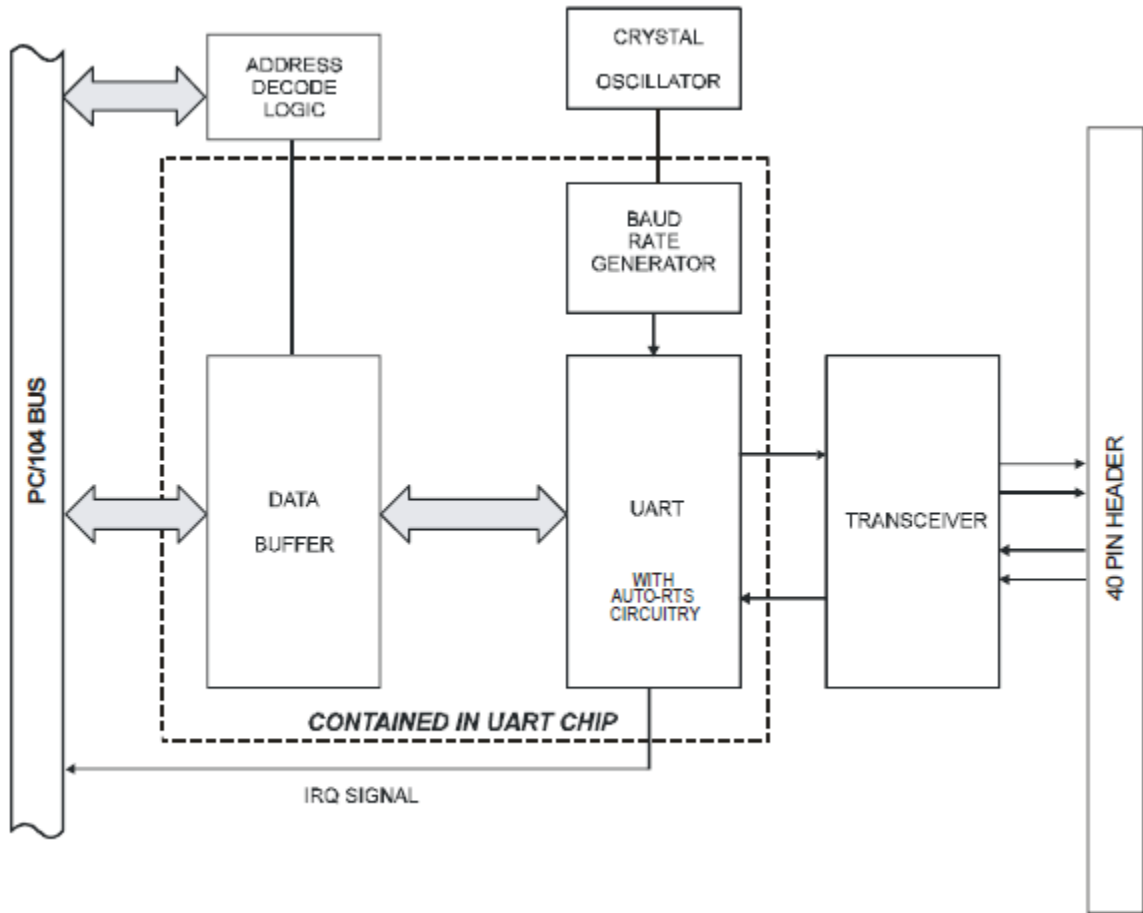[48]   "Sensor Description," [Online]. Available: http://www.ufa.cas.cz/html/upperatm/DSS_Description_&_protokol.pdf.

Appendices

Appendix A: MATLAB Simulation Code input and output guide.

1) Control
   a) PD.m
      i) input: time, desired quaternion and current state vector
      ii) output: 3x1 magnetorquer moment vector
   b) Stabilizer.m
      i) Input: Current state vector and geomagnetic vector
      ii) Output: 3x1 magnetorquer moment vector
2) Determination
   a) EKF.m
      i) Input: time and time step size
      ii) Output: 7x1 state vector
   b) intEKF.m
   c) LowPass.m
      i) Input: count number and old estimated state vector
      ii) Output: new estimated state vector
   d) TRIAD_est.m
      i) Input: time
      ii) Output: estimated state vector
3) Math
   a) angle_diff.m
      i) input: two column vectors x1 and x2
      ii) output: angle difference in radian between the two input vectors
   b) angular_error.m
      i) input: sun position vector, angular error type and error angle
      ii) output: point error angle
   c) dcm_from_q.m
      i) input: quaternion (either 4x1 or 1x4)
      ii) output: 3x3 directional cosine matrix
   d) delta_q.m
      i) input: two column quaternions: desired and actual in form of {k,j,i,1}
      ii) output: a unit vector given the difference between the quaternions
   e) q_from_dcm.m
      i) input: direction cosine matrix
      ii) output: quaternion
   f) q_to_ypr.m
      i) input: a row quaternion matrix
      ii) output: a row matrix containing yaw pitch and roll angles in radian
   g) QXx_ypr.m
      i) input: yaw pitch and roll angles in radian
      ii) output: directional cosine matrix
   h) Wx_to_wypr.m
      i) input: angular velocity measurement matrix and 3x1 vector of yaw pitch and roll angles
      ii) output: body frame velocity
   i) ypr_to_q.m
      i) input: 3x1 vector of yaw pitch and roll angles
      ii) output: 4x1 quaternion

4) Models (it contains similar algorithm as in sensors, but it produces the model for each parameter)
   a) model_desq.m
      i) input: time
      ii) output: desired quaternion of the satellite
   b) model_magnet.m
      i) input: time and mode (real for measurement with noise)
      ii) output: real strength of magnet field vector
   c) model_nadir.m
      i) input: time, mode (real for measurement with noise), frame (body for satellite body frame) and form (Quat for converted quaternion output)
      ii) output: quaternion of the satellite's motion relative to the nadir
   d) model_sun.m
      i) input: time and mode (real for measurement with noise)
      ii) output: sun vector model
5) Sensors
   a) sensor_gyro.m
      i) input: mode (ideal for original system, real for noise corrupted system)
      ii) output: real or ideal angular velocity vector
   b) sensor_magnet.m
      i) input: time, mode (real for measurement with noise) and frame (body for satellite body frame)
      ii) output: magnetometer measurement from pre-generated data from STK
   c) sensor_sun.m
      i) input: time, mode (real for measurement with noise) and frame (body for satellite body frame)
      ii) output: angular error of the sun sensor
      iii) note: when the angle is out of the field of view of the fine sun sensor, the angular error becomes larger
6) Main folder
   a) inertia.m
      i) input: CubeSat unit and x, y, z positions of the cg point
      ii) Output: inertia tensor
   b) jacobian.m
      i) input: none
      ii) output: Jacobian matrix

Appendix B: Connector Map for ADL LX8PC-AMD Geode LX800

Ref-No.	Function
U303*	"Memory"
P600	"Serial Interface COM1"
P601	"USB 1 to 4, LAN, Sound"
P602	"Serial Interface COM2"
P603	"Parallel Interface LPT"
P604	"IDE Interface"
P606	"LCD"
P900	"System"
P901	"PC/104-Bus"
P902	"PC/104-Bus"
P903	"Power Supply"
P904	"SMBus"
P905	"Monitoring Functions"
P906	"PC/104-Plus Bus"
P907	"VGA"
P1000	"Fan"

Appendix C: Functional Diagram for Accesio 104-COM-8SM

Appendix D: Connection Layout Diagram for Diamond-MM-32-AT I/O
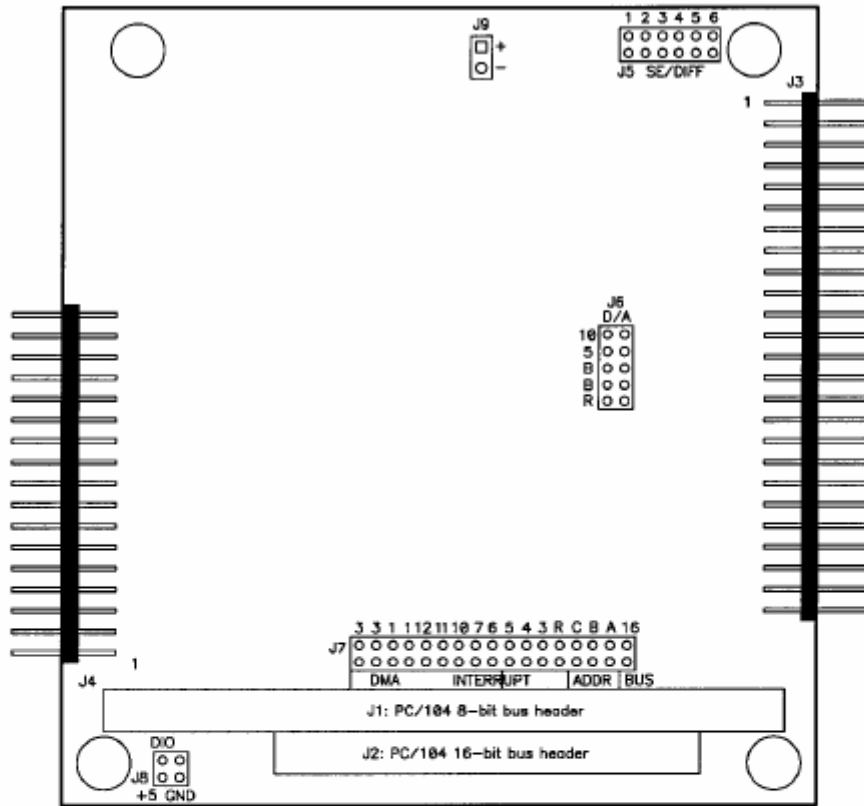
Legend

J1	PC/104 8-bit bus header
J2	PC/104 16-bit bus header (only used for interrupt level)
J3	Analog I/O header (includes trigger and ctr/timer signals)
J4	Digital I/O header
J5	Analog input single-ended / differential configuration
J6	D/A unipolar / bipolar / full-scale range configuration
J7	Base address / DMA level / interrupt level / bus width
J8	Digital I/O pull-up / pull-down configuration
J9	Test connector; not used in normal operation